Climatology of Tracked Persistent Maxima of 500-hPa Geopotential Height

Ping Liu[1], Yuejian Zhu[2], Qin Zhang[3], Jon Gottschalck[3], Minghua Zhang[1], Christopher Melhauser[6], Wei Li[6], Hong Guan[7], Xiaqiong Zhou[6], Dingchen Hou[2], Malaquias Peña[6], Guoxiong Wu[4], Yimin Liu[4], Linjiong Zhou[5], Bian He[4], Wenting Hu[4], Raymond Sukhdeo[1]

1. School of Marine and Atmospheric Sciences, Stony Brook University, Stony Brook, New York 11794-5000, USA

2. Environmental Modeling Center, NCEP/NOAA/NWS, USA

3. Climate Prediction Center, NCEP/NOAA/NWS, USA

4. LASG, IAP, Beijing, P. R. China

5. GFDL, NOAA, USA

6. IMSG at Environmental Modeling Center, NCEP/NWS/NOAA, USA

7. SRG at Environmental Modeling Center, NCEP/NWS/NOAA, USA

Corresponding author:

Dr. Ping Liu, ORCID # 0000-0002-6828-8878

Endeavor Hall 199, SoMAS, Stony Brook University

Stony Brook, New York, 11794-5000 USA, Email: ping.liu@stonybrook.edu

Abstract

Persistent open ridges and blocking highs (maxima) of 500-hPa geopotential height (Z500; PMZ) adjacent in space and time are identified and tracked as one event with a Lagrangian objective approach to derive their climatological statistics with some dynamical reasoning. A PMZ starts with a core that contains a local eddy maximum of Z500 and its neighboring grid points whose eddy values decrease radially to about 20 geopotential meters (GPMs) smaller than the maximum. It connects two consecutive cores that share at least one grid point and are within 10 degrees of longitude of each other using an intensity-weighted location. The PMZ ends at the core without a successor. On each day, the PMZ impacts an area of grid points contiguous to the core and with eddy values decreasing radially to 100 GPMs.

The PMZs identified and tracked consist of persistent ridges, omega blockings and blocked anticyclones either connected or as individual events. For example, the PMZ during 2-13 August 2003 corresponds to persistent open ridges that caused the extreme heatwave in Western Europe. Climatological statistics based on the PMZs longer than three days generally agree with those of blockings. In the Northern Hemisphere, more PMZs occur in DJF season than in JJA and their duration both exhibit a log-linear distribution. Because more omega-shape blocking highs and open ridges are counted, the PMZs occur more frequently over Northeast Pacific than over Atlantic-Europe during cool seasons. Similar results are obtained using the 200-hPa geopotential height (in place of Z500), indicating the quasi-barotropic nature of the PMZ.

Keywords Tracking · Open Ridge · Anticyclone · Blocking · Persistence · Climatology

1 Introduction

Fluctuations of 500-hPa geopotential height (Z500 hereafter) dynamically steer surface weather systems in middle latitudes. For example, a Z500 maximum indicating a ridge or an anticyclone induces a local surface high pressure system that generally causes benign, dry and warm weather (Hoskins and Woollings 2015; Horton et al. 2016). Under favorable conditions, such as when it resides in a jet-exit region (Pelly and Hoskins 2003; Tyrlis and Hoskins 2008; Masato et al. 2013a; Davini et al. 2014; Faranda et al. 2016; O'Reilly et al. 2016), the local Z500 maximum tends to persist and develop into an atmospheric blocking episode. The jet stream is subsequently split into two branches that can persist for several days to weeks (Rex 1950). Consequently, dry and warm surface conditions can be prolonged and potentially lead to severe droughts and heatwaves, especially during the summer (Green 1977; Dole et al. 2011; Horton et al. 2016). Identifying and tracking persistent maxima of Z500 (PMZ hereafter) is essential in understanding and predicting their onset, prolonged duration, subsequent dissipation, and their impact on local, upstream and downstream weather and regional climate.

Atmospheric blocking patterns are traditionally recognized as blocked highs with established reversals of meridional pressure gradients, and they are methodologically separated from open ridges with little signature of the reversal although both systems are closely connected in dynamics (e.g., Rex 1950; Lejenäs and Økland 1983; Tibaldi and Molteni 1990; Pelly and Hoskins 2003; Masato et al. 2013a). It has been found that open ridges at Z500 in certain cases can induce harmful weather such as the extreme heatwave in early August 2003 over Europe (Black et al. 2004) and a cold event in East Asia (Bueh and Xie 2015), but generally have not been tracked as systematically as conventional blockings. A survey of existing blocking indices below indicates a lack of methods that incorporate open ridges, revealing a need for an algorithm for tracking the PMZ events consisting of traditional blocking highs and persistent open ridges and for deriving the climatological statistics of PMZs.

Existing blocking indices can be grouped based on the type of the base field and specific blocking situations (Barriopedro et al. 2010). Commonly used base fields include the Z500 (Tibaldi and Molteni 1990; Barriopedro et al. 2006; Barriopedro et al. 2010; Masato et al. 2013b; Faranda et al. 2016), the meridional wind component (Kaas and Branstator 1993), the local stream function computed using spherical harmonics expansion (Metz 1986), the vertically averaged potential vorticity (Schwierz et al. 2004; Small et al. 2014), and the potential temperature at the 2-PVU (potential vorticity unit) surface near the dynamical tropopause (Pelly and Hoskins 2003; Masato et al. 2013a, b).

Blocking situations can divide the indices into four categories: (1) a regional and persistent reversal of meridional gradients in the absolute field of Z500 or potential temperature (e.g., Lejenäs and Økland 1983; Tibaldi and Molteni 1990; Pelly and Hoskins 2003; Barriopedro et al. 2006; Diao et al. 2006; Scherrer et al. 2006; Barriopedro et al. 2010; Masato et al. 2013a and b; Faranda et al. 2016; Schiemann et al. 2017) which, through the geostrophic relationship or the PV invertibility principle (Hoskins et al. 1985) is dynamically equivalent to easterly flows in place of westerly around a reference latitude representative of the jet stream. A benefit of the reversal approaches is their dynamical link to the breaking of Rossby waves and to the reversed flow inhibiting further Rossby wave propagation (Faranda et al. 2016); (2) persistent positive departures from the climatological Z500 or negative departures of the PV field (e.g., Dole and

Gordon 1983; Shukla and Mo 1983; Knox and Hay 1985; Sausen et al. 1995; Schwierz et al. 2004; Renwick 2005; Dunn-Sigouin et al. 2013; Faranda et al. 2016; Parsons et al. 2016); (3) eddy fields identified as areas bounded by southerly wind upstream and northerly downstream (Kaas and Branstator 1993; Cash and Lee 2000) or as regions where the Z500 largely exceeds the zonal mean of a surrounding sector (Hartmann and Ghan 1980; Mullen 1986; 1989); and (4) atmospheric circulation patterns associated with weather regimes objectively derived from either statistical multivariate methods (Vautard 1990; Michelangeli et al. 1995) or neural networks (Verdecchia et al. 1996).

The most commonly used blocking indices can be simplified into two types based on the absolute or anomalous base field. The first type uses the absolute field of Z500 (Lejenäs and Økland 1983; Tibaldi and Molteni 1990; TM90 hereafter; D'Andrea et al. 1998; Scherrer et al. 2006; Masato et al. 2013b; Davini and D'Andrea et al. 2016; Schiemann et al. 2017) and of potential temperature (Pelly and Hoskins 2003; PH03 hereafter; Masato et al. 2013a; Small et al. 2014). The TM90 index follows the classic definition of blocking by Rex (1950), emphasizing the existence of a persistent and appreciable split flow into a double jet with a sharp transition from westerly to meridional flow. They adapted the original criteria of Rex (1950) into an objective method to provide a measure of the westerly flow at each longitude from the meridional difference of Z500 gradients centered at a constant reference latitude. This index can provide instantaneous blocking detection based on the longitude of westerly flow reversal. TM90 added a gradient criterion of Z500 to filter out some systems that marginally meet the requirement. Additionally, the method was generalized to consider spatial and temporal characteristics by setting the thresholds for a minimum number of consecutive blocked longitudes. The TM90 index, however, has some limitations due to (1) its longitudinal (i.e., 1-D) description of blocking, (2) the fixed central reference latitude at which the meridional gradient is computed, and (3) the predefinition of blocking sectors.

The limitations of the TM90 index can be reduced by refining the definition of regional blocking (PH03; Masato et al. 2013a and b). PH03 argued that atmospheric blocking may be described as the wave breaking of potential temperature (θ) on a potential vorticity (PV) surface near the dynamical tropopause and the subsequent reversal of the meridional gradients of θ. They constructed a dynamical blocking index using the meridional θ difference on the 2-PVU surface, representing a Rossby wave breaking regime (Chen et al. 2015; Huang and Nakamura 2016). The revised index (known as the PV-θ index) corresponds to the central blocking reference latitude (CBL) that varies with longitude and is located where the climatological high-pass transient eddy kinetic energy reaches a maximum. As a result, the PV-θ index identifies the annual average location of Pacific blocking closer to the Northeast Pacific. Additional improvements to TM90 have been made by a 2-D expansion that avoids a priori definition of blocking sectors, such as over Atlantic or Europe (Barriopedro et al. 2006; Diao et al. 2006; Scherrer et al. 2006; Masato et al. 2013a, b; Athanasidis et al. 2014).

The second type of commonly used blocking index is time-anomaly based (Dole and Gordon 1983; DG83 hereafter; Sausen et al. 1995; Sinclair 1996; Doblas-Reyes et al. 2002; Renwick 2005; Dunn-Sigouin et al. 2013; Parsons et al. 2016). The DG83 follows Elliot and Smith (1949) to identify persistent patterns as positive and negative Z500 anomalies from the climatological mean that exceed a given threshold for a prescribed duration. Variants of DG83 detect blockings as persistent positive anomalies (PPA; Sinclair 1996) that are larger than 100 GPMs in Z500 (Renwick 2005) or 8 hPa in mean sea level pressure (Parsons et al. 2016) and persist for at least 5 days (Renwick 2005; Parsons et al. 2016). Another more recent anomaly-based blocking index uses potential vorticity anomalies vertically integrated from the mid-troposphere to the lower stratosphere (Schwierz et al. 2004; Small et al. 2014). That index tends to identify more occurrences during the summer compared to other indices including those based on only Z500 anomalies. These anomaly-based indices provide a full 2-D spatial (longitude-latitude) description of blocking, which is helpful for regional applications.

There are limitations for anomaly-only-based blocking indices as well. They generally require that the time series of the base field are sufficiently long to derive an estimation of the mean (e.g., DG83; Sausen et al. 1995; Doblas-Reyes et al. 2002; Renwick 2005; Parsons et al. 2016), which is difficult for operational predictions. In addition, the threshold of positive anomalies alone appears insufficient to define a Rex blocking (e.g., Liu 1994; Sausen et al. 1995), because the position of the anomaly center can also be a critical parameter. In some cases, positive anomalies may correspond to weakened troughs more closely than blocking patterns (e.g., Charney et al. 1981).

The limitations of the full field or anomaly-based blocking indices can be reduced by combining their strengths and using Z500 as the base field (e.g., Barriopedro et al. 2010). Blockings are viewed as 2-D anomalies capable of reversing the meridional gradients of geopotential heights, thus removing the condition of meridional inversion in both the total field and the anomaly threshold. Such a combined index exhibits agreement with the climatological regions of maximum band-pass filtered height variance and simultaneous wave amplification. The detected blockings, however, retain some limitations associated with time anomalies to be discussed more below. Masato et al. (2013b) designed another 2-D blocking index based on daily mean Z500 that uses the varying central blocking latitude (CBL) of PH03. This index equally evaluates equatorward cutoff lows and poleward blocking highs as a disruption to westerlies, which agrees with the wave-breaking methodology of PH03. The resultant blocking climatology is more consistent with PH03 as well (their Fig. 1a).

From the various blocking indices previously discussed, it can be generally concluded that a mature blocking pattern is the target of these indices with open ridges generally excluded (e.g., Fig. 2 in PH03; Fig. 2 in Barriopedro et al. 2010; Fig. 1 in Masato et al. 2013a). Such a separation poses some limitations of existing blocking indices in recognizing the importance of persistent ridges, immature blockings and omega-shape blocks. Additionally, on weather maps, omega-shape blockings are commonly observed, preceded and succeeded by persistent open ridges in the Northeast Pacific impacting the weather and regional climate over North America. Missing such meaningful systems in statistics tends to narrow the causes of harmful weather and climate events.

This study attempts to answer the outstanding question: What and how different statistics would persistent open ridges and blocking highs demonstrate when they are identified and tracked as one event if they are adjacent in both time and space? Motivated by the blocking indices based on meridional winds (or eddy fields; Kaas and Branstator 1993), the time anomalies of Z500 (e.g., DG83; Renwick 2005; Dunn-Sigouin et al. 2013; Parsons et al. 2016) and the objective detection for tilted ridges (Bueh and Xie 2015), this study attempts to develop a new approach to identify and track both blocking anticyclones and persistent open ridges as persistent maxima at Z500 (PMZs) and derive their climatological statistics with some dynamical reasoning, ignoring the cut-off low component of a traditional blocking pattern. Section 2 introduces the data, compares the Z500 eddy component with different anomalies, demonstrates its advantage over time anomalies for detecting open ridges, and describes the Lagrangian objective approach for identifying and tracking PMZs based on instant daily zonal anomalies. Section 3 presents the results of three case studies including the European heatwaves in early August 2003, the climatological statistics of tracked PMZ events as well as comparisons with those of persistent positive anomalies (PPA; Renwick 2005; Parsons et al. 2016) and blockings. Section 4 summarizes the new findings and discusses some caveats in the new algorithm.

2 Data and Methodology

2.1 Data

The daily data are produced by the NCEP-NCAR Reanalysis project (Kalnay et al. 1996) including 500-hPa geopotential height (Z500), surface temperature, and 200-hPa geopotential height (Z200). All fields cover 1 January 1979-31 December 2015 at a resolution of 2.5°×2.5° in longitude and latitude. This data set has been widely used for detecting blocking episodes in previous studies (e.g., Renwick 2005; Barriopedro et al. 2006; Barriopedro et al. 2010; Davini et al. 2014; Colucci and Kelleher 2015; Sousa et al. 2017). The Z500 fields from the ERA-Interim reanalysis (Dee et al. 2011; Athanasiadis et al. 2014) are used for testing the sensitivity of tracked PMZs to data resolution. These data have a native resolution of 0.75°×0.75° and are interpolated to 1.0°×1.0°, 1.125°×1.125°, 1.5°×1.5°, 2.0°×2.0° , 2.5°×2.5° and 3°×3° covering the same time period.

2.2 Decomposing the Daily Z500 in Time and Longitude

Open ridges and closed anticyclones at Z500 are positive anomalies after subtracting the zonal mean of each latitude circle. Their longitudinal locations are determined by the southerly flow on the west side and northerly on the east in the Northern Hemisphere (Kaas and Branstator 1993). The eddy anomalies of Z500 after removing the zonal mean retain the relative magnitude of a ridge or anticyclone, and thus retain the location of meridional flows based on the geostrophic relationship. Time anomalies tend to deviate from a ridge or anticyclone because the subtracted climatology is not purely zonal. To demonstrate that eddy anomalies follow the ridges in the full field more closely than time anomalies, we can decompose the Z500 (Z in short in the following equations) following Peixoto and Oort (1992) as

$$Z = \bar{Z} + Z' = [Z] + Z^* = [\bar{Z}] + [Z]' + \bar{Z}^* + Z^{*\prime}, \qquad (1)$$

where the overbar and brackets are for averages in time and longitude, respectively, and the superscript prime and star indicate the transient and zonally deviated eddy fields. The time mean (i.e., climatology of $\bar{Z}$) consists of the long-term mean and the first four harmonics of the annual cycle[1] during 1979-2015. The conventional time anomaly, Z', includes transient zonal mean $[Z]'$ and transient eddy anomaly $Z^{*\prime}$, but not a time-mean

[1] A forward Fourier transform produces the harmonics with periodicities at 365, 182, 121, and 91 days. A backward transform based on these components as well as the long-term mean forms the time mean.

eddy $\bar{Z}^*$ component which contains a large portion of zonal inhomogeneity. Thus, time anomaly (anomaly for short) Z' can be written as

$$Z' = Z - \bar{Z} = Z - [\bar{Z}] - \bar{Z}^*. \quad (2)$$

From (2), it can be reasoned that positive Z' anomalies can potentially deviate away from a ridge in Z and a moderately positive area or maximum of Z' can correspond to a weakened trough of Z. This deviation sometimes can be large, as demonstrated by the composite maps of Z500 and its different anomalies (Fig. 1). Figure 1 shows the averaged Z500 (color shading) of a tracked PMZ containing a segment of omega blocking during 9-26 January 2013. An enhanced ridge in Z (red shading) is evident close to the north Pacific coast of North America with a weaker ridge over the southeast coast of the U.S. Conventional Z500 anomalies Z', represented by gray contours, have a primary local maximum near 145^{o}W and 50^{o}N that deviates from the ridge of Z by 15-20° to the west; the anomaly associated with the weaker ridge west of 90^{o}W and near 35^{o}N corresponds to a weakened trough. Maximum anomalies of Z' agree less well with blocking ridges in either geographical location or magnitude. Some adjustments in the Z' would be needed to well represent these ridges.

When the climatological eddy $\bar{Z}^*$ is retained, another type of eddy anomaly Z_a can be derived (Peixoto and Oort 1992) as

$$Z_a = Z' + \bar{Z}^* = [Z]' + Z^{*\prime} + \bar{Z}^* = Z - [\bar{Z}]. \quad (3)$$

The maximum Z_a (green contours in Fig. 1) follows the ridge more closely and the maximum has a much larger amplitude than Z' for the shallow ridge near the southeast coast of the U.S.

For identifying and tracking the PMZ that emphasizes zonal inhomogeneity without defining and computing the climatology $\bar{Z}$, the transient zonal mean $[Z]'$ can be discarded from (3) to quantify the daily eddy anomalies as

$$Z^* = Z - [Z] = \bar{Z}^* + Z^{*\prime}. \qquad (4)$$

Daily eddy anomalies Z^* (eddy anomalies hereafter; contours in black in Fig. 1) are consistent with Z_a, and even more closely follow the location and amplitude of a ridge as well as the flow patterns on a daily Z500 map (Fig. 1). In addition, discarding only zonal averages ensures that a positive Z^* corresponds to a ridge and not a weakened trough. The transient zonal average $[Z]'$ was excluded implicitly through meridional geostrophic winds in the blocking index of Kaas and Branstator (1993). Of the three anomalies, Z^* best represents both the spatial and magnitude characteristics of the open ridges and omega-shape blockings of Z500. Also because its derivation is instantaneous and does not require long-term records for computing the climatology as in the Z', it is chosen as the base field for identifying and tracking the PMZ.

2.3 Identifying and Tracking the Cores of PMZ

An idealized PMZ event has a life cycle consecutively consisting of open ridges, omega-shape blockings, closed anticyclones, omega-shape blockings and open ridges with possibly different persistent time and moving speed. Our approach is intended to identify these components represented by maximum Z* as objects (referred to as cores below) and track them into PMZ events if they are adjacent in both time and space. This approach is Lagrangian, different from an Eulerian method which examines the meridional geostrophic winds (Z*; Kaas and Branstator 1993), Z' (Renwick 2005) or MSLP' (Parsons et al. 2016) on individual grid point.

To identify and track the PMZ, the first step is to remove the zonal average $[Z]$ at each latitude from the daily Z500 following Equation (4) and identify the local maxima of the eddy field Z^* as possible candidates for a PMZ episode. These maxima are screened automatically to locate local extremes or cores. The innermost layer of the core includes a center point and eight surrounding points with Z^* values smaller than or equal to that of the center. This condition ensures that the center is closed, which is potentially helpful for regional applications. The inner core then expands to include more points immediately connected with the nine points. Their Z* values are larger than or equal to a small positive value (100 GPMs in this study), but slightly (at most 20 GPMs in this study) smaller than that of the center and decrease radially. The 100-GPM threshold appears in Fig. 1 as the outer-most closed contour (black) for the stronger ridge and the only closed contour for the shallow ridge. Tests indicate that this threshold and slightly different values can help remove very shallow ridges with positive Z*, but does not affect closed highs or stronger ridges (not shown). A much larger threshold of 200 GPMs will be shown to substantially reduce the number of tracked PMZs. The 20-GPM threshold encloses a sufficiently large number of points while making the cores on the same day sufficiently small and easily separable. Slightly modifying this threshold (e.g., within 17.5-22.5 GPMs) does not substantially change the results (not shown). A wider range of the thresholds, including 10, 30, and 50 GPMs, will substantially increase or reduce the number of PMZs (to be discussed below).

Figure 2 shows a snapshot of the cores on 9 January 2013 at the start of a PMZ episode. It also indicates how closely the core represents an open ridge or a blocking anticyclone. Colored contours are for the full field of Z500 and black contours for the eddy anomaly Z^*; both have an interval of 100 GPMs. The gray-shading indicates a core that will have been tracked as a part of a PMZ. A total of three cores are identified on this day. The first one is located near 155°W and 50°N with a black cross; it starts the PMZ episode as an enhanced ridge. The black cross represents the intensity-weighted location of core points. It is clearly collocated with the Z500 ridge and indicates that the algorithm can identify a core for an open ridge. The second core is over Europe and extends into the northeast Atlantic, corresponding to a blocked high near 10°W and 65°N. The third core corresponds to a ridge near 10°E and 60°N. There are other Z^* maxima following ridges in the Southern Hemisphere, but are not identified as PMZ cores. Using prescribed thresholds, it is clear from Fig. 2 that PMZ cores can be detected objectively and ensure that the identified cores of Z^* are indeed ridges or closed anticyclones.

The second step is to track the evolution of PMZ cores. After all cores are identified, each of them is compared with those on successive eddy anomaly Z^*maps. Two cores on two consecutive maps are deemed connected if they share at least one grid point in common. This single criterion can include weak maxima that enclose too many grid points and move too fast. To exclude such cases, the distance between the mass-weighted locations of two cores is chosen to be within 10 degrees of longitude. The 10-degree threshold is based on the discussions found in previous studies (DG83, TM90, PH03 and Barriopedro et al. 2010) for the scale of a typical blocking and the characteristic velocity of travelling large-scale disturbances, which is on the order of 10–15 degrees longitude per day (e.g. Treidl et al. 1981). A PMZ event in this study is then defined as connected cores lasting for 4 days or longer, although a smaller number of days can be used for an approximate comparison with the instantaneous blockings identified by blocking indices (e.g., TM90; PH03; Renwick 2005; Masato et al. 2013a, b; Parsons et al. 2016). An individual PMZ event is objectively defined as finished when the core is no longer connected with a successor.

2.4 Expanding the Tracked Cores

After all PMZ events are identified and tracked from 1 January 1979 to 31 December 2015, each tracked core is expanded to include additional grid points for time-evolving impact areas. We use 100 GPMs again as the threshold for additional points immediately connected with the core points. This threshold is based on the composite in Fig. 1 (black contours) and can be reduced to any positive value to exclude weak ridges according to Equation (4). Each grid point belongs to one PMZ core to avoid double counting. Figure 3 shows the snapshots of the expanded PMZs (gray shading) during 9-26 January 2013. All gray areas are collocated with the maxima of Z^* and closely follow open ridges and subsequent omega-shape blocking episodes. It is noteworthy that the ridge existed as early as 6 January 2013 (shown as the black contours), but it is not identified and tracked as a part of the PMZ until three days later. This case supports the reasonable treatment of connected open ridges and blocking highs as one PMZ event.

The steps and criteria for tracking a PMZ event are summarized below.

• A core is identified to include a local maximum of eddy anomaly Z^* and its neighboring grid points whose values are greater than 100 GPMs and decrease radially to about 20 GPMs smaller than the maximum value.

• Two cores on consecutive Z^* maps belong to a PMZ event if they share at least one grid point and move no greater than 10 degrees longitude per day.

• The PMZ persists for four days or longer and ends at the core without a successor. The number of days can be as small as two.

• Each of the tracked cores is expanded to include more contiguous points whose Z^* values decrease radially to about 100 GPMs excluding weak ridges.

Because time anomalies Z' are capable of detecting ridges even though their maximum can deviate away from actual ridges in the Northeast Pacific (Fig. 1 and Fig. 8b below), Table 1 gives comparisons of Z*-based PMZ approaches and Z'-based blocking indices, which are inferred from DG83 and Renwick (2005).

3. Results

3.1 Three Cases

To demonstrate how open ridges and blocking highs form one event, the PMZ episode that occurred during 9-26 January 2013 – discussed in previous section and illustrated in Figs. 2-3 – is examined in more detail. Open ridges had preceded this episode for several days (Fig. 3a), but moved faster than the threshold of 10 degrees longitude per day[2]. After 9 January (Fig. 2), the ridge became sufficiently stationary. Over the next 4 days, it gradually strengthened and developed into an omega-shape blocking (Fig. 3c). The blocked ridge then weakened and tilted to the northwest, but remained quasi-stationary. By 22 January (Fig. 3e), the ridge opened and its core was inland with the impact area (gray shading) extending into the central U.S. It moved slightly faster over the next several days, reaching the central U.S. by 26 January. The open ridge stayed over the U.S. for two more days, but moved faster than the threshold and thus not tracked.

The average 2-m temperature anomaly[3] (T_s'; Fig. 4) during the blocking episode 9-26 January 2013 demonstrates how the abnormally warm conditions in the Northwest U.S.-Canada was modulated by the PMZ event. The temperature was above normal along the outer edge of the omega blocking with the largest anomaly of as much as 6 K to the north of the ridge and in the average core area. It was below normal to the northeast of the 100-GPM Z^* contour (this also supports 100 GPMs as a threshold for the impact area of the PMZ). The cold anomaly was located at downstream of the ridge (thick-gray dashed contours). This temperature anomaly pattern is a typical response to omega-shape blockings (e.g., Konard 1996). The warmer conditions in the central and eastern U.S. correspond to a weakened trough and a shallow ridge (indicated by marginally positive Z^*), with the southeast U.S. experiencing a period of positive anomalies. Figure 4 indicates that the temperature anomalies align with the maximum eddy of Z500, supporting Z^* as a suitable metric for tracking PMZ episodes.

[2] Some of the open ridges can be included in the PMZ event using a larger speed as threshold.
[3] Ts' derived by a formula similar to (2).

The second PMZ case is associated with the extreme heatwave in Europe during early August 2003 (Black et al. 2004). It was exceptionally warm and dry from May through the end of August that year. The heatwave in early August was particularly serious in Western Europe. The warm and dry summer season was attributed to persistent anomalous anticyclonic flow patterns in the lower and middle troposphere (Black et al. 2004). Our tracking algorithm identified and tracked three PMZ events during the three months (PMZ details shown in Table 2). The first two events covered the whole month of June 2003 and the third occurred 2-13 August 2003, the episode that contributed to the extreme heatwave.

Figure 5 shows the averaged 2-m temperature anomalies over 2-13 August 2003. Warm anomalies exceeded 8 K in Western Europe, which corresponded to the center of the extreme heatwave. This center was collocated with the Z500 ridge (thick-gray); it also coincided with the center of the Z^*. The PMZ episode is successfully identified and tracked by our approach (Fig. 6). The Z500 ridges were shallow and open during this period, a setup difficult to be tracked as a conventional blocking pattern (Rex 1950). For example, there was little evident reversal of pressure gradients associated with Z500 ridges, thus the TM90 index would ignore this feature as a blocking. Specifically, on 2 August, the core (black cross) was located near 48^{o}N and 5^{o}E and then only shifted slightly eastward by a couple of degrees during the next 4-5 days (red crosses). This allowed for the buildup of hot and dry surface conditions. The core moved northward and was located over the United Kingdom on 8 August when the S-shaped inner contour indicated a weak reversal of Z500 gradients. This would be classified as an instantaneous blocking by the TM90 index. It subsequently became a wide open ridge and moved further to the northeast approximately 58^{o}N on 10 August when the United Kingdom was located right behind the ridge and Reading experienced its hottest day (Black et al. 2004). On 12 August, the core (black cross) moved back to Northern France when Paris had record-breaking temperatures. The gray-shaded impact area of the tracked PMZ in Fig. 6 wholly covered Western Europe, coinciding with the anomaly patterns of surface temperature (Fig. 5).

The third PMZ case occurred from 8 to 18 February 1994, which included a blocking anticyclone over Europe. The blocking episode was detected by existing blocking indices (Barnes et al. 2012; their Fig. 1). We show it here to demonstrate that this blocking episode was in fact preceded by open ridges and an omega-shape blocking, and it eventually decayed back into an omega-shape blocking. The PMZ was a highly dynamic event that persisted longer than the event detected by the existing blocking indices. In addition, some differences between the location of maximum Z^* and that of reversed Z500 gradients can be discerned.

Figure 7 shows this PMZ event during 8-18 February 1994. On 8 February (Fig. 7a), the Z^* core sits right on the head of the Z500 ridge and its impact area (gray shading) encloses the ridge, branching slightly northeastward to the prime meridian. Further to the northeast between 10^{o}E and 30^{o}E and near 60^{o}N, there was a decaying ridge which would be detected as an instantaneous blocking by the TM90 index. This ridge is identified by our algorithm, but it is not tracked as a persistent event because its duration was less than 4 days (not shown). Two days later, the tracked ridge strengthened and moved northward by a couple of degrees (Fig. 7b). The impact area extended up to 80^{o}N, absorbing the decayed blocking. The gray shading was connected with the shallow ridge north of the

Caribbean, which can be interpreted as separate systems. By 12 February, the connection was completely broken and the Z^* core (Fig. 7c) developed into a classical omega-shape blocking and moved into northeast Europe. On 14 February, a strong blocked anticyclone as well as a weak cutoff low at (0^{o}E, 50^{o}N) formed a classical blocking pattern (e.g., Barnes et al. 2012) with the Z^* core located near 15^{o}E and 70^{o}N. The anticyclone gradually weakened and moved faster southeastward and by 18 February, it decayed back into a weak omega-shape blocking with the core approaching 45^{o}E and 50^{o}N (Fig. 7f). The life cycle of this PMZ event shown in Fig. 7 demonstrates that the evolution of a dynamic blocking highs on the full field Z500 from developing to decaying stages can be well identified and tracked with the maxima of eddy field Z^*.

3.2 Climatological Statistics

In this section, we present the climatological statistics of tracked PMZ events in terms of their cores and expanded impact grid points. Since blocking highs are the major part of persistent events, especially over the Atlantic-Europe sector, the statistics below will be approximately compared with those for blocking patterns reported in previous studies (e.g., Kaas and Branstator 1993; PH03; Barriopedro et al. 2010; Masato et al. 2013b). Meanwhile, positive persistent anomalies (PPA) in time as blockings of Renwick (2005) are reproduced for a comparison in more detail.

The first climatological statistics are the annual frequency distribution for the impact grid points of the PMZ events from 1979-2015 (color shading in Fig. 8a) superimposed by climatological Z500 ($\bar{Z}$ in Eq. 1; black contours in Fig. 8a). In the Northern Hemisphere, two sectors have annual occurrence frequencies above 18%

(darker yellow). One is in the eastern Atlantic-Europe and the other in northwest North America, with the maximum value closely following climatological ridges (cf. maximum $\bar{Z}^*$ in Fig. 8b). This two-dimensional spatial pattern of the frequency distribution generally agrees with that of blocking patterns in other studies (e.g., PH03; their Fig. 7; Barriopedro et al. 2010; their Fig. 7). The occurrence frequency magnitude of the PMZs over the Pacific-America sector, however, is notably different. The center here is above 21%, relatively stronger than the one in the Atlantic-Europe sector. In contrast, previous studies except Kaas and Branstator (1993) (e.g., PH03) reported that the Atlantic-Europe sector has much larger annual occurrence frequencies for blocking patterns. In addition, the center of PMZs is inland near 120°W and 50°N, substantially different from the center of blocking patterns generally found over the northeast Pacific or even closer to the date line (e.g., Barriopedro et al. 2010; their Fig. 7). Such differences indicate that a large number of persistent ridges and blockings were previously undetected, many occurring closer to the northwest coast of North America. In both sectors, PMZ events occur at different latitudes. This agrees with the varying reference latitudes widely used for detecting blockings since PH03 (e.g., Masato et al. 2013b). In the Southern Hemisphere, the occurrence of PMZ is much larger in the Eastern Hemisphere, with a center between 150°E and 160°W and near 55°S with an approximate magnitude of 12-15%. A secondary center is close to 50°E and 40°S with a magnitude less than 9%. Both centers follow shallow ridges closely (cf. maximum $\bar{Z}^*$ in Fig. 8b). It is noteworthy that the yearly numbers of PMZs have a slight decreasing trend but statistically insignificant in 1979-2015, and they do not show a clear relationship with ENSO (not shown).

In several indices, blockings were considered equivalent to the persistent positive anomalies (PPA) in time (DG83; Renwick 2005; Parsons et al. 2016) imposed with some thresholds. For a comparison with the method in this study, the PPAs of Z500 were diagnosed from 1979 to 2015 based on the NCEP-NCAR Reanalysis data (color shading in Fig. 8b). The thresholds for PPAs are similar to those in Renwick (2005), i.e., positive anomalies larger than 100 GPMs and persistent for 5 days and longer. This selection makes the results relatively more comparable with those for the PMZs (Fig. 8a vs. Fig. 8b in color shading). In the Southern Hemisphere, the annual frequencies of PPA exceed 15% (yellow) in (150°W-90°W, 50°S-70°S), similar to those based on MSLP (Sinclair 1996; Parsons et al. 2016, area framed in red in their Fig. 1a). This area corresponds to relatively weaker Z500 ridges (smaller positive $\bar{Z}^*$); it is farther eastward than the shallow climatological ridges as maximum $\bar{Z}^*$ near the date line. Such a deviation is more evident in the Northeast Pacific where relative maximum PPA frequencies exceeding 12% deviate by about 20 degrees in longitude west of the climatological ridge (maximum $\bar{Z}^*$ over the inland of northwestern North America). Similar deviations remain in the composite of the Z500 conditioned on the detected PPA for each grid point (not shown). It is noteworthy that the blocking frequency is also larger in the Northeast Pacific than inland North America detected by a combination of TM90 and DG83 (Barriopedro et al. 2010; their Fig. 7), indicating similar deviations associated with time anomalies. In addition, PPA frequencies remain notably large in high latitudes. For example, the values exceed 12% (yellow) in more than half of the high latitudes in the Northern Hemisphere. Such large values potentially overestimate blocking frequencies (Liu 1994) and can be improved by constraining the calculation with additional conditions such as requiring reversals in meridional pressure gradients (Barriopedro et al. 2010). These two limitations of PPA based on time anomalies are much less evident in PMZs based on eddy anomalies. For example, the PMZ frequency center is collocated with the climatological ridges inland of the northwest America (Fig. 8a). Because of these limitations, other statistics of the PPA are not compared with PMZs below.

Blocking-pattern occurrences have a strong seasonality with a maximum in DJF and a minimum in JJA (e.g., PH03; Masato et al. 2013b). The tracked Z500 persistent maxima in this study also have a maximum occurring in DJF and a minimum in JJA. During DJF seasons (Fig. 9a), the overall pattern for the occurrence is similar to the annual distribution (Fig. 8), although there are notable differences. The first is that the maximum frequency occurs along the northwest coast of North America with a magnitude larger than 36%, while the second maximum is over the eastern Atlantic and Western Europe with a magnitude less than 28%. This relationship is similar to that for blockings only using meridional geostrophic winds (Kaas and Branstator 1993; their Fig. 2a), but opposite to other blocking indices in which the Atlantic has the largest frequency in DJF in the Northern Hemisphere with values 30-50% larger than those in the northeast Pacific (e.g., PH03; Barriopedro et al. 2010; Masato et al. 2013b). It is noteworthy the PMZ frequency maximum in the northwest coast of North America is still about 15% larger than that of only blockings detected by meridional geostrophic winds (equivalent to Z*; Kaas and Branstator 1993). Over the Greenland, however, the frequencies of PMZs are smaller than those of blocking patterns reported in other studies. For example, a close inspection of DJF frequencies indicates that the PMZs occur 3-4% in the Southwest Greenland and 8-10% in the Southeast, both about 5% in absolute value smaller than the blockings (e.g., Scherrer et al. 2006; their Fig. 2; Davini et al. 2014; the left panel of their Fig. 1) but slightly larger than the large-scale blocking events in Athanasiadis et al. (2014; their Fig. 4). Causes of such differences merit further investigation. Focusing on the Southern Hemisphere, the occurrence frequencies in DJF have an increase approximately 5% near the central Pacific with a slight change in other regions compared with the annual occurrences.

PMZ events have the smallest occurrence frequency during JJA in most of the Northern Hemisphere (Fig. 9b). Three centers with a maximum occurrence exceeding 12% are evident. The first is over the central-eastern Atlantic near 25^{o}W and 45^{o}N, the second stretches across Europe and extends to 60^{o}E with two local maxima, and the third is located in the northwest U.S. at 100^{o}W and 45^{o}N. Compared with the annual distribution, the largest drop in frequency occurs over the northwest coast of North America by more than 14% with a shift of the center further inland. A similar large drop occurs in the Atlantic-Europe sector by as much as 14%. The only increase of frequency occurs in the Russian Far East with a positive center of 4-7% near 60^{o}N and 130^{o}E. This is the location where blocking highs usually occur to anchor the wet period during late June and July known as Meiyu in China, Baiwu in Japan, or Changma in Korea (e.g., Chen and Zhai 2015). In the Southern Hemisphere, the occurrence frequency is generally enhanced by 4-7% between 30^{o}S and 80^{o}S, indicating more PMZ events in cool seasons as well.

During the MAM season (not shown), there is a large drop in frequency of up to 6% over the northwest coast of North America compared to the annual distribution, while the change is very small over the Atlantic-Europe sector. In central Asia, there is an increase of up to 8% over the annual frequency near 80^{o}E and 45^{o}N. A small change in occurrence frequency occurs in the Southern Hemisphere. During the SON season (not shown) it is very close to the annual, except for a slight reduction in Northeast Pacific, central Asia, and the Atlantic, and a small increase over northern Europe.

From the frequency distributions of DJF and JJA seasons, it can be concluded that PMZ events occur mostly between 40-60 degrees in latitude in both hemispheres. The frequencies averaged at the three latitudes of 40^o, 50^o, and 60^{o}N in each season are shown in Fig. 10 to further illustrate the seasonal variation of PMZ occurrences with longitude. The thick-black curve for the annual distribution has maximum values of 16-18% at 120^{o}W and near 30^{o}W-13^{o}E, corresponding to the northeast Pacific and Atlantic-Europe sectors (cf. Fig. 8a). In DJF season, the maximum in northeast Pacific near 120^{o}W exceeds 33%, larger than that in Atlantic-Europe near 15^{o}W-10^{o}E of 25-27%, which is the most outstanding finding by our approach. The MAM season is close to the annual distribution except for a small 3% increase between 40^o-60^{o}E. The JJA season has the lowest frequency magnitude among the seasons and annual mean, with the maxima dropping below 10%. The SON season is most similar to the annual distribution. The seasonality in Fig. 10 is evident, with DJF exhibiting the maximum and JJA the minimum occurrence frequency.

We next present the climatological occurrence frequencies of tracked PMZ events in longitude, latitude, intensity, duration, and average moving speed. The core points of each PMZ are used for these statistics such that the results will be approximately compared with those for blocking patterns in previous studies (e.g., PH03; Barriopedro et al. 2010; Masato et al. 2013b).

Figure 11 shows the total number of PMZ cores during 1979-2015. In the Northern Hemisphere, PMZ cores occur most frequently in the eastern Pacific between 130^{o}-110^{o}W with a second maximum over the northeast Atlantic and Europe between 30^{o}W-10^{o}E. These two maxima in occurrence frequency agree with those for blocking patterns in previous studies (e.g., PH03), despite the maximum in the Atlantic-Europe sector for blocking patterns being larger than that in Pacific. The number of occurrences drops in other longitudes and close to zero around 120^{o}E. In the Southern Hemisphere, the occurrence frequency is more homogenous although several longitudes have a slightly larger number of events near 30-60^{o}E, 150-160^{o}E, and around 60^{o}W. Such homogeneity is likely associated with the larger ocean coverage in the Southern Hemisphere. In addition, the core points fall between 30-85° latitude in both Northern and Southern Hemispheres. The maximum number of occurrences is near 50^{o}N in the Northern Hemisphere and 57.5^{o}S in the Southern Hemisphere, supporting 50^{o}N as the reference for identifying blocking patterns in the TM90 index (PH03).

The durations of blockings are known to have a log-linear distribution (e.g., PH03). Figure 12 shows a similar distribution for PMZ cores. The tracked PMZ cores in the Southern Hemisphere (green in Fig. 12) have lower numbers as expected with a faster rate of decrease compared with the Northern Hemisphere. However, they share a similar relative distribution in both hemispheres, and after taking the logarithm, the distributions become nearly linear (Fig. 12b). The Southern Hemisphere has an increased negative slope indicating a faster decrease in occurrences over time.

The average intensity of tracked cores does not have a log-linear distribution and is similar between hemispheres (not shown). It is worth noting that the weak ridges of

Z500 are filtered out from the distributions by using the Z^* threshold of 100 GPMs. A smaller threshold will add more cores, but does not substantially change the intensity distributions, partly because the maximum number of PMZ core events occurs near the 200 GPMs intensity (not shown).

Most of the tracked PMZ cores move slower than 7 degrees in longitude per day, as shown in Fig. 13. In the Northern Hemisphere, about 75% of the cores move slower than 4 degrees per day (black in Fig. 13) and all of the cores has an average speed of 2.8 degrees per day. In the Southern Hemisphere (green in Fig. 13), the cores move slightly faster with an average speed of 3.4 degrees per day. Since 3-4 degrees per day (4-5 m s^{-1}), is much smaller than the mean zonal wind speed at 500 hPa (about 20-30 m s^{-1}), these cores are overall quasi-stationary. The low core speed supports the 10 degrees per day as a reasonable threshold.

3.3 Comparison with Z200

Small et al (2014) argued that the low occurrence frequency of blocking patterns in JJA can be attributed to the Z500 which is used as the base field for tracking. Since our algorithm has identified more occurrences of PMZ events than blocking patterns (cf. Fig. 8), a comparison is made between the persistent maxima of Z500 with those at 200 hPa (Z200) to see whether substantially more PMZ events can be identified and tracked during JJA seasons.

The PMZs of Z200 were identified and tracked using the procedure described in Section 2. The only difference is that a threshold of 150 GPMs of Z^* is used to define the core points and impact area. This relatively larger value of 150 GPMs consistently removes weak maxima, which are mostly associated with the subtropical anticyclones over the Tibetan Plateau during summer. An even larger value, (e.g., 200 GPMs) substantially reduces the number of cores, but the relative frequency of persistent maxima is still smaller in JJA than in DJF. Here we show only the occurrence frequency distributions averaged at 40^o, 50^o and 60^{o}N (Fig. 14). The overall patterns are nearly identical to those in Fig. 10. A careful inspection indicates that the occurrence of the persistent maxima of Z200 in JJA is overall larger than that of Z500. For example, it is nearly 15% around 60^{o}E, much larger than that of Z500 of less than 9%. This is consistent with Small et al. (2014) being that more PMZ events can be detected in the upper troposphere in JJA. Nevertheless, the larger values in the Pacific and Atlantic-Europe sectors are still much smaller than those in DJF, which does not change the strong seasonality. The similar distribution of the persistent maxima of Z500 and Z200 also reflects the quasi-barotropic nature of the PMZ events, similar to that of blockings (e.g., PH03).

3.4 Sensitivity to Data Resolution and PMZ Thresholds

Tracked PMZ characteristics can vary with data resolution and the thresholds set in the tracking algorithm (cf. Table 1). The probable range of the characteristics can be specified by independently controlling these factors and analyzing their impact on the algorithm performance. The first test employs seven resolutions for the daily Z^* of the ERA-Interim Reanalysis (Dee et al. 2011; ERAI hereafter), while it retains the same PMZ thresholds in Table 1. Results show that the PMZ features vary slightly at coarser resolutions and more dramatically as the resolution increases. This sensitivity is well represented by the changes of PMZ numbers per year and PMZ frequencies (Table 3 and Fig. 15).

Table 3 compares the number of PMZ events per year and the STD in eight cases. The PMZ counts per year and STD in both Southern and Northern Hemispheres are similar for the data resolutions of 1.5°×1.5° to 3°×3°, indicating small sensitivity at coarser resolutions. At 0.75°×0.75°, the number per year slightly decreases in the Southern Hemisphere, while it decreases more dramatically (3-4%) in the Northern Hemisphere. Also compared in Table 3 is the average traveling distance of PMZ events (measured by degrees longitude). The distances vary within 1-2% (less than half a degree longitude) among all resolutions, indicating a small sensitivity to grid spacing.

The PMZ frequency varies with data resolution as well, as shown by the annual frequency distribution for the PMZ impact areas averaged at 40^o, 50^o and 60^oN (closest latitudes otherwise) latitude (Fig. 15). The frequency changes slightly between 10^o-90^oE, and it remains nearly identical at other longitudes at coarser data resolutions (2.5°~3°; black, red, and green curves in Fig. 15). Increasing the data resolution causes the frequency to drop by 3-5% at 1.5°×1.5° and 5-9% at 0.75°×0.75° over the Atlantic and Pacific-North America sectors (cf. Table 3). This drop is partially due to a smaller area being covered by the set of grid points at higher resolutions. A close inspection of Fig. 15, however, indicates that the overall spatial distribution remains similar among all tested resolutions, with the frequency slightly larger in the Northeastern Pacific-North America sector compared to that in the Atlantic-Europe sector.

The second sensitivity test prescribes a wider range of PMZ thresholds at a fixed data resolution of 2.5°×2.5°. Two thresholds in the algorithm with large ranges are tested in reference to the control (CTL) case based on Table 1, i.e., within 20 GPMs (threshold 1) smaller than the local maximum for the cores and the 100 GPMs (threshold 2) for both the cores and impact areas. Tracked PMZ features fluctuate with these thresholds more dramatically, as shown in Table 4 for the number of PMZ events per year and in Fig. 16 for the average annual frequencies of PMZ impact areas. Increasing threshold 1 from 20 (CTL) to 30 (C30) or 50 (C50) GPMs reduces PMZ numbers per year by 20-40% (Table 4). In contrast, decreasing threshold 1 to 10 GPMs (C10) increases PMZs 4% in the Southern Hemisphere and 25% in the Northern Hemisphere. Increasing threshold 2 from 100 to 200 GPMs for the impact area (E200) does not change the number of PMZs per year, but it reduces the frequency by ~50% (light blue in Fig. 19). Increasing threshold 2 to 200 GPMs for both the cores and impact areas (B200) reduces both PMZ numbers per year (Table 4) and frequencies (purple in Fig. 16) by more than 50%. The STD of the number per year reduces with increasing thresholds as well. A careful inspection of Fig. 16 indicates that the change in frequencies is spatially dependent, changing slightly differently in the Atlantic-Europe and Pacific-North America sectors (color curves in Fig. 16). In particular, the C10 (red) case increases the tracked PMZ frequency by 3% over the Atlantic-Europe sector while it decreases the frequency very slightly over the Northeastern Pacific-North America sector. The relatively larger sensitivity over the Atlantic-Europe sector is likely due to an increased number of smaller PMZ cores being identified. It is noteworthy that the frequency distributions are generally similar among the cases, with slightly larger values in the Northeastern Pacific-North America sector compared to the Atlantic-Europe sector. Similar sensitivities of PMZ features to data resolution and subjective thresholds occur in other seasons (not shown). These tests indicate that the 2.5°×2.5° resolution and associated subjective thresholds (specified in Section 2) are reasonable configurations for identifying and tracking the PMZs.

4 Summary and Discussions

In this study, a Lagrangian objective approach is developed to identify and track persistent open ridges of 500-hPa geopotential height (Z500) either as an individual event or as a part attached to a blocking anticyclone. These ridges are not designed to be captured by most indices for only blockings. It is found that the eddy anomalies Z^* of Z500 closely follow open ridges and closed anticyclones and thus a suitable base field for the tracking algorithm.

Based on daily eddy anomalies Z^*, the algorithm identifies local maximum cores as candidates for tracking. A threshold of 100 GPMs is prescribed to filter out shallow ridges. After the cores are identified, they are examined on consecutive daily Z^* maps. Two cores belong to one PMZ event as long as they share at least one grid point and their intensity-weighted central locations are within 10 degrees in longitude.

The tracked PMZ events have a few unique features, besides their similarity to blocking patterns, as shown by three case studies and climatological statistics. Main results using the new method are summarized. Firstly, it was found that persistent open ridges coincided with the historical heatwave in Europe during early August 2003. This event includes nearly all open ridges and a short and weak blocking. These systems are generally not intended for detection by an index for blocking patterns only, but they were identified and tracked by the method in this study. Secondly, in climatological statistics, PMZ events have a much larger number of occurrences in northeast Pacific and northwest North America during cool seasons compared to the number of blocking patterns detected by several blocking indices (e.g., Kaas and Branstator 1993; PH03; Masato et al. 2013b). This feature is identified for the first time. The increased number of PMZs is attributed to the persistent open ridges and weak omega-shape blockings identified using our approach. Finally, the climatological statistics for PMZs are generally consistent with those for blocking patterns, agreeing with the definitions of Z^* and blocking highs as a subset of PMZs. A comparison of the persistent maxima at Z500 with that at Z200 indicates that the number of occurrence remains smaller in summer than that in winter. There appears to be a strong seasonality and quasi-barotropic aspect of PMZs.

The algorithm in this study uses several subjective thresholds. The two most influential are the moving speed limit at 10 degrees longitude per day and the persistence of 4 days. Both are selected following similar values in several blocking indices (e.g., TM90; PH03). Other thresholds are fundamentally less critical, because positive eddy anomalies Z^* correspond to only ridges. Slightly different thresholds such as moderately reducing the 100 GPMs of eddy anomaly Z^* for all PMZ grid-point values do not substantially change the results, especially the relative larger frequency of the Northeastern Pacific sector. There is some sensitivity in tracked PMZs to data resolution, as indicated by the ERA-Interim products. Using higher resolution reanalysis data appears to reduce PMZ frequencies, because 1) the Z* at higher resolutions tend to split the cores at coarse resolutions into smaller centers making the thresholds for PMZs more difficult to meet, and 2) less grid points are counted in PMZ impact areas. If the resolutions are the same at 2.5°×2.5°, the tracked PMZs are nearly identical in the ERA-Interim and the NCEP-NCAR Reanalysis, suggesting a fair approach for comparison. The PMZ number and frequencies are reduced dramatically with largely elevated thresholds. Increasing the threshold from ≤ 20 to ≤ 50 GPMs for the cores reduces PMZ numbers by 40% and increasing the threshold from 100 to 200 GPMs for both the core and impact areas reduces PMZ frequencies by 50%.

This method treats open ridges and blocking highs in a unified framework, thus, as few as two consecutive days of regularly gridded Z500 maps are sufficient for the algorithm to start the tracking procedure. There is no need for a long time series of the base field to derive the estimation of the mean and its time anomalies. This feature makes it easy and feasible to evaluate operational systems with short reforecasts and to validate short-term numerical simulations. Treating open ridges and blockings at onset, developing, mature, and decaying stages as one system may be favorable for understanding how and why open ridges evolve into blocking episodes. It can also be a caveat for applications requiring the separation of blocking patterns from persistent open ridges if they are actually independent. This separation is difficult by the Z* itself as the core is closed for any type of PMZ. A constraint with strong meridional geostrophic winds (Kaas and Branstator 1993) or a combination of our algorithm with the TM90 index appears promising and merits more investigation.

Acknowledgments

P. Liu, L. Zhou, W. Hu, B. He, and R. Sukhdeo were partially supported by the National Weather Service under the grant NA15NWS4680015. M. Zhang was supported by the Office of Biological and Environmental Research of the US Department of Energy and by the National Science Foundation. G. Wu, Y. Liu, and P. Liu were partially supported by the NSFC under the grant 91437219. B. He, W. Hu and P. Liu were partially supported by the NSFC under the grant 41405091 and 41305065. NCEP-NCAR Reanalysis data provided by the NOAA/OAR/ESRL PSD, Boulder, Colorado, USA, from their Web site at http://www.esrl.noaa.gov/psd/.

References

Athanasiadias PJ, Bellucci A, Hermanson L, Scaife AA, MacLachlan C, Arribas A, Materia S, Borrelli A, Gualdi S (2014) The representation of atmospheric blocking and the associated low-frequency variability in two seasonal prediction systems. J Clim 27:9082-9100

Barnes EA, Slingo J, Woollings T (2012) A methodology for the comparison of blocking climatologies across indices, models, and climate scenarios. Clim Dyn 38:2467-2481

Barriopedro D, Garcia-Herrera R, Lupo AR, Hernandez E (2006) A climatology of Northern Hemisphere blocking. J. Clim 19:1042-1063

Barriopedro D, Garcia-Herrera R, Gonzalez-Rouco JF, Trigo RM (2010) Application of blocking diagnosis methods to general circulation models. Part I: a novel detection scheme. Clim Dyn. 35:1373-1391

Black E, Blackburn M, Harrison G, Hoskins B, Methven J (2004) Factors contributing to the summer 2003 European heatwave. Wea 17:4080-4088

Bueh C, Xie Z (2015) An objective technique for detecting large-scale tilted ridges and troughs and its application to an East Asian cold event. Mon Wea Rev 143:4765-4783

Cash BA, Lee S (2000) Dynamical processes of block evolution. J Atmos Sci 57:3202-3218

Charney JG, Shukla J, Mo KC (1981) Comparison of a barotropic blocking theory with observation. J Atmos Sci 38:762-779

Chen G, Lu J, Burrows DA, Leung LR (2015) Local finite-amplitude wave activity as an objective diagnostic of midlatitude extreme weather. Geophys Res Lett 42:10952-10960

Chen Y, Zhai P (2015) Synoptic-scale precursors of the East Asia/Pacific teleconnection pattern responsible for persistent extreme precipitation in the Yantze River Valley. Q J R Meteorol Soc 141:1389-1403

Colucci SJ, Kelleher ME (2015) Diagnostic comparison of tropospheric blocking events with and without sudden stratospheric warming. J Atmos Sci 72:2227-2240

Davini P, Cagnazzo C, Fogli PG, Manzini E, Gualdi S, Navarra A (2014) European blocking and Atlantic jet stream variability in the NCEP/NCAR reanalysis and the CMCC-CMS climate model. Clim Dyn 43:71-85

Davini P, D'Andrea F (2016) Northern Hemisphere atmospheric blocking representation in global climate models: twenty years of improvements? J Clim 29:8823-8840

D'Andrea F, Tibaldi S, Blackburn M, Boer G, Déqué M, Dix MR, Dugas B, Ferranti L, Iwasaki T, Kitoh A, Pope V, Randall D, Roeckner E, Straus D, Stern W, Van den Dool H, Williamson D (1998) Northern Hemisphere atmospheric blocking as simulated by 15 atmospheric general circulation models in the period 1979-1988. Clim Dyn 14:385-407

Dee DP, Uppala SM, Simmons AJ, Berrisford P, Poli P, Kobayashi S, Andrae U, Balmaseda MA, Balsamo G, Bauer P, Bechtold P, Beljaars ACM, Van de Berg L, Bidlot J, Bormann N, Delsol C, Dragani R, Fuentes M, Geer AJ, Haimberger L, Healy SB, Hersbach H, Hólm EV, Isaksen L, Kållberg P, Köhler M, Matricardi M, McNally AP, Monge-Sanz BM, Morcrette JJ, Park BK, Peubey C, De Rosnay P, Tavolato C, Thépaut JN, Vitart F (2011) The ERA-Interim reanalysis: configuration and performance of the data assimilation system. Q J R Meteorol Soc 137:553-597

Diao Y, Li J, Luo D (2006) A new blocking index and its application: blocking action in the northern hemisphere. J Clim 19:4819-4839

Doblas-Reyes FJ, Casado MJ, Pastor MA (2002) Sensitivity of the Northern Hemisphere blocking frequency to the detection index. J Geophy Res 107:D2 4009 10.1029/2000JD000290

Dole RM, Gordon ND (1983) Persistent anomalies of the extratropical Northern Hemisphere wintertime circulation: Geographical distribution and regional persistence characteristics. Mon Wea Rev 111:1567-1586

Dole RM, Hoerling M, Perlwitz J, Eischeid J, Pegion P, Zhang T, Quan XW, Xu T, Murray D (2011) Was there a basis for anticipating the 2010 Russian heat wave? Geophys Res Lett 38:L06702 doi:10.1029/2010GL046582

Dunn-Sigouin E, Son SW, Lin H (2013) Evaluation of Northern Hemisphere blocking climatology in the Global Environment Multiscale (GEM) model. Mon Wea Rev 141:707-727

Elliot RD, Smith TB (1949) A study of the effect of large blocking highs on the general circulation in the northern hemisphere westerlies. J Meteor 6:67-85

Faranda D, Masato G, Moloney N, Sato Y, Daviaud F, Dubrulle B, Yiou P (2016) The switching between zonal and blocked mid-latitude atmospheric circulation: a dynamical system perspective. Clim Dyn 47:1587-1599

Green JSA (1977) The weather during July 1976: Some dynamical considerations of the drought. Wea 32:120-126

Hamill TM, Bates GT, Whitaker JS, Murray DR, Fiorino M, Galarneau TJJr., Zhu Y, Lapenta W (2013) NOAA's second-generation global medium-range ensemble reforecast data set. Bull Amer Meteor Soc 94:1553-1565 doi: http://dx.doi.org/10.1175/BAMS-D-12-00014.1

Hartmann DL, Ghan SJ (1980) A statistical study of the dynamics of blocking. Mon Wea Rev 108:1144-1159

Horton RM, Mankin JS, Lesk C, Coffel E, Raymond C (2016) A review of recent advances in research on extreme heat events. Curr Clim Change Rep 2:242-259

Hoskins BJ, McIntyre ME, Robertson A (1985) On the use and significance of isentropic potential vorticity maps. Q J R Meteor Soc 111: 877-946

Hoskins BJ, Woollings T (2015) Persistent extratropical regimes and climate extremes. Curr Clim Change Rep 1:115-124

Huang CSY, Nakamura N (2016) Local finite-amplitude wave activity as a diagnostic of anomalous weather events. J Atmos Sci 73:211-229 doi:10.1175/JAS-D-15-0194.1

Kaas E, Branstator G (1993) The relationship between a zonal index and blocking activity. J Atmos Sci 50**:**3061-3077

Kalnay E, Kanamitsu M, Kistler R, Collins W, Deaven D, Gandin L, Iredell M, Saha S, White G, Woollen J, Zhu Y, Chelliah M, Ebisuzaki W, Higgins W, Janowiak J, Mo K, Ropelewski C, Leetmaa A, Reynolds R, Jenne R (1996) The NCEP/NCAR 40-year reanalysis project. Bull Am Meteor Soc 77:437–471

Knox JL, Hay JE (1985) Blocking signatures in the northern hemisphere: frequency distribution and interpretation. J Climatol 5:1-16

Konard CEII (1996) Relationships between the intensity of cold-air outbreaks and the evolution of synoptic and planetary-scale features over North America. Mon Wea Rev 124:1067-1083

Lejen*ä*s H, Økland H (1983) Characteristics of northern hemisphere blocking as determined from long time series of observational data. Tellus 35A:350-362

Liu Q (1994) On the definition and persistence of blocking. Tellus 46A:286-290

Masato G, Hoskins BJ, Woolings TJ (2013a) Wave-breaking characteristics of Northern Hemisphere winter blocking: A two-dimensional approach. J. Clim 26:4535-4549

Masato G, Hoskins BJ, Woolings TJ (2013b) Winter and Summer Northern Hemisphere blocking in CMIP5 models. J Clim **26:**7044-7059 doi:10.1175/JCLI-D-12-00466.1

Metz W (1986) Transient cyclone-scale vorticity forcing of blocking highs. J Atmos Sci 43:1467-1483

Michelangeli P, Vautard R, Legras B (1995) Weather regimes: Reoccurrence and quasi-stationarity. J Atmos Sci 52:1237-1256

Mullen SL (1986) The local balances of vorticity and heat for blocking anticyclones in a spectral General Circulation Model. J Atmos Sci 43:1406-1441

Mullen SL (1989) Model experiments on the impact of Pacific sea surface temperature anomalies on blocking frequency. J Clim 2:997-1013

O'Reilly C, Minobe S, Kuwano-Yoshida A (2016) The influence of the Gulf Stream on wintertime European blocking. Clim Dyn 47:1545-1567

Parsons S, Renwick JA, McDonald AJ (2016) An assessment of future Southern Hemisphere blocking using CMIP5 projections from four GCMs. J. Clim 29:7599-7611

Peixoto JP, Oort AH (1992) Physics of Climate. American Institute of Physics 520 pp

Pelly JL, Hoskins BJ (2003) A new perspective on blocking. J Atmos Sci 60:743-755 doi:10.1175/1520-0469(2003)060,0743:ANPOB.2.0.CO;2

Renwick JA (2005) Persistent positive anomalies in the Southern Hemisphere circulation. Mon Wea Rev 133:977-988

Rex DF (1950) Blocking action in the middle troposphere and its effect upon regional climate. I. An aerological study of blocking action. Tellus 2:196-211

Sausen R, Konig W, Sielmann F (1995) Analysis of blocking events observation and ECHAM model simulations. Tellus 47A:421-438

Scherrer SC, Croci-Maspoli M, Schwierz C, Appenzeller C (2006) Two-dimensional indices of atmospheric blocking and their statistical relationship with winter climate patterns in the Euro-Atlantic region. Int J Climatol 26:233-249

Schiemann R, Demory ME, Shaffrey LC, Strachan J, Vidale PL, Mizielinski MS, Roberts MJ, Matsueda M, Wehner MF, Jung T (2017) The resolution sensitivity of Northern Hemisphere blocking in four 25-km atmospheric global circulation models. J Clim 30:337–358 doi: 10.1175/JCLI-D-16-0100.1

Schwierz C, Croci-Maspoli M, Davies HC (2004) Perspicacious indicators of atmospheric blocking. Geophys Res Lett 31:L06125 doi:10.1029/2003GL019341

Shukla J, Mo KC (1983) Seasonal and geographical variation of blocking. Mon Wea Rev 111:388-402

Sinclair MR (1996) A climatology of anticyclones and blocking for the Southern Hemisphere. Mon Wea Rev 124:245-263

Small D, Atallah E, Gyakum JR (2014) An objectively determined blocking index and its Northern Hemisphere climatology. J. Clim 27:2948-2970

Sousa P, Trigo RM, Barriopedro D, Soares PMM, Ramos AM, Liberato MLR (2017) Responses of European precipitation distributions and regimes to different blocking locations. Clim Dyn 48:1141-1160

Tibaldi S, Molteni F (1990) On the operational predictability of blocking. Tellus 42:343-365

Treidl, RA, Birch EC, Sajecki P (1981) Blocking action in the Northern Hemisphere: a climatological study. Atmos Ocean 19:1-23

Tyrlis E, Hoskins BJ (2008) Aspects of Northern Hemisphere atmospheric blocking climatology. J Atmos Sci 65:1638-1652

Vautard R (1990) Multiple weather regimes over the North Atlantic: analysis of precursors and successors. Mon Wea Rev 118:2056-2081

Verdecchia M, Visconti G, D'Andrea F, Tibaldi S (1996) A neural network approach for blocking recognition. Geophys Res Lett 23:2081-2084

Table 1 Comparisons of Z*- and Z'-based approaches

Parameters and Diagnosis	**Z*-based PMZ**	**Z'-Based blockings**
Full base field	500-hPa geopotential height (Z500)	Z500
Z500 temporal resolution	Daily	Twice daily
Z500 horizontal resolution	2.5°×2.5°	5°×5°
Time of the year	All seasons, 1979-2015	Winter (90 days), 1963-76
Spatial coverage	Global	Northern Hemisphere
Anomaly definition	Removal of zonal mean	Removal of climatology
Low-pass filtering	No	Periods shorter than 6 days
Normalized anomalies	No	By latitude
Spatial filtering	No	9-point
Length of record	≥ 2 days	Long record for climatology
Raw anomaly signs	Positive only	Both positive and negative
Raw anomaly systems	Positive for ridge only	Positive possible for a trough Negative possible for a ridge
Raw maximum and ridge locations	Coincide closely	Deviated by ~10-15° longitude over Northeastern Pacific
Tracking	Lagrangian	Lagrangian
Tracking object	Closed local maxima as cores	Above local threshold every 50 up to 250 GPMs
Threshold for a core	100 GMPs; within 20 GPMs of maxima	Maxima not separate
Threshold for impact area	100 GPMs	Above local threshold every 50 up to 250 GPMs
Moving speed	≤ 10° longitude per day	Stationary for blockings
Days of persistence	≥ 4 but can be 2 days	≥ 5 up to 25 days
Extension	2-dimensional (2-D)	2-D
Description	2-D PMZ	2-D blocking (positive)

Table 2 Three tracked PMZ events impacting Europe during JJA 2003

Starting Date	Duration (days)	Mean central latitude (°N)	Mean central longitude (°E)	Mean Intensity (GPMs)
2003/05/28	18	52.5	13.0	182.3
2003/06/18	12	54.6	1.4	170.2
2003/08/02	12	51.7	4.4	162.3

Table 3 Average number of cores per year and STD, average traveling distance (degrees longitude) of PMZs versus data resolution using the same PMZ thresholds (Table 1)

Data Source	Resolution	Cores/year and STD				Average distance	
		SH[1]		NH		SH	NH
NCEP-NCAR	2.5° × 2.5°	67.5	8.8	100.6	9.3	17.4°	19.3°
ERA-Interim	2.5° × 2.5°	68.8	8.2	98.8	7.3	17.7°	19.1°
ERA-Interim	3° × 3°	66.4	8.4	96.2	8.8	17.8°	19.3°
ERA-Interim	2° × 2°	69.7	7.4	100.4	7.8	17.7°	19.4°
ERA-Interim	1.5° × 1.5°	68.8	7.4	98.8	8.0	17.8°	19.3°
ERA-Interim	1.125° × 1.125°	66.8	5.8	94.9	7.3	17.7°	19.5°
ERA-Interim	1° × 1°	65.8	5.1	93.9	7.5	17.6°	19.6°
ERA-Interim	0.75° × 0.75°	64.8	6.1	91.5	7.9	17.3°	19.6°

[1] The SH is for the Southern Hemisphere and NH for the Northern Hemisphere.

Table 4 Sensitivity of average cores per year and STD of PMZ events to the thresholds for the core or expanded area

Name of case	Thresholds		Cores/year and STD			
	Core	Expanded	SH		NH	
CTL	100 GPMs; within 20 GPMs	100 GPMs	67.5	8.8	100.6	9.3
C10	100 GPMs; within 10 GPMs	100 GPMs	70.0	10.0	125.8	9.5
C30	100 GPMs; within 30 GPMs	100 GPMs	46.9	6.6	77.8	8.2
C50	100 GPMs; within 50 GPMs	100 GPMs	32.2	6.9	59.7	7.6
E200	Same as CTL	200 GPMs	67.5	8.8	100.6	9.3
B200	200 GPMs; within 20 GPMs	200 GPMs	28.6	4.8	43.5	6.6

Figure Caption List

Fig. 1 500-hPa geopotential height (color shading in every 100 GPMs), two types of anomalies (contours) with (Z_a; green) or without (Z'; gray) climatological eddies, and daily eddies (Z^*; black) over Northeast Pacific and North America averaged during the PMZ episode in 9-26 January 2013. Contour interval is 50 GPMs with 0 being omitted.

Fig. 2 A snapshot on 9 January 2013 for the identified maxima (gray shading) of different PMZ episodes. Contours in color or black are for the total field Z500 or Z* (starting from 100 GPMs) with an interval of 100 GPMs. The black cross indicates the intensity-weighted location of starting center in the northeast Pacific.

Fig. 3 Successive snapshots of intensity-weighted locations of PMZ cores during 9-26 January 2013. Black cross represents the core of current day and red ones for its predecessors, and gray shading is for the impact area of the PMZ on current day. Color contours are for the Z500 every 100 GPMs.

Fig. 4 Anomalies of 2-m temperature (color shading in K; T_s'), total 500-hPa geopotential height (gray-thick dashed isopleths; every 100 GPMs with the 5800 isopleth labeled; Z500), and daily eddies (black contours; Z^*) averaged during the blocking episode from 9-26 January 2013.

Fig. 5 Same as Fig. 4, but for the blocking episode associated with the record heatwave in Western Europe during 2-13 August 2003.

Fig. 6 Same as Fig. 3, but for persistent strong open ridges that occurred 2-12 August 2003 and caused the record heatwave in Western Europe.

Fig. 7 Same as Fig. 3, but for a PMZ episode that evolved from an open ridge to an omega-shape blocking, a cutoff high, and decayed back into an omega-shape blocking during 8-18 February 1994.

Fig. 8 Annual frequency distributions (color shading) for (a) the impact grid points of tracked PMZ events and (b) PPA days during all seasons from 1979-2015 super-imposed with all-time climatology in black contours for (a) Z500 starting at 5800 GPMs with an interval of 100 GPMs and (b) eddy anomalies Z* of (a) with an interval of 20 GPMs.

Fig. 9 Frequency distributions for the impact area of tracked PMZ events in DJF (a) and JJA (b).

Fig. 10 Frequency distribution for the impact grid points of the tracked PMZ events between 1979-2015 for annual (solid black), seasonal DJF (black dashed), MAM (red), JJA (green), and SON (blue) averaged at the three latitudes of 40^{o}, 50^{o}, and 60^{o}N.

Fig. 11 Total number of PMZ cores during 1979-2015.

Fig. 12 Duration distributions for tracked PMZ events in the Northern (black) and Southern (green) Hemisphere during all seasons in 1979-2015. Panels (a) and (b) are for the total number of cores and its natural logarithm, respectively.

Fig. 13 Frequency distributions of averaged moving speed (degree in longitude per day) for tracked PMZ cores in the Northern (black) and Southern (green) Hemisphere during all seasons in 1979-2015.

Fig. 14 Same as Fig. 10, but for the Z200 where the threshold of the core and impact grid points is 150 GPMs.

Fig. 15 Annual frequency distribution averaged at the three latitudes of 40^o, 50^o, and 60^oN (closest latitudes otherwise) for the impact grid points of the tracked PMZ events between 1979-2015 based on the Z500 from the NCEP-NCAR Reanalysis at 2.5°×2.5° in longitude and latitude (black), ERA-Interim at 0.75°×0.75° (brown), 1.0°×1.0° (light blue), 1.125°×1.125° (purple), 1.5°×1.5° (light blue), 2.0°×2.0° (blue), 2.5°×2.5° (red), and 3°×3° (green), respectively.

Fig. 16 Sensitivity to the thresholds in the annual frequency distribution averaged at the three latitudes of 40^o, 50^o, and 60^oN for the impact grid points of the tracked PMZ events between 1979-2015 based on the Z500 from the NCEP-NCAR Reanalysis at 2.5°×2.5° in longitude and latitude for CTL (black), C10 (red), C30 (green), C50 (blue), E200 (light blue), and B200 (purple), respectively. See Table 4 for the thresholds in each case.

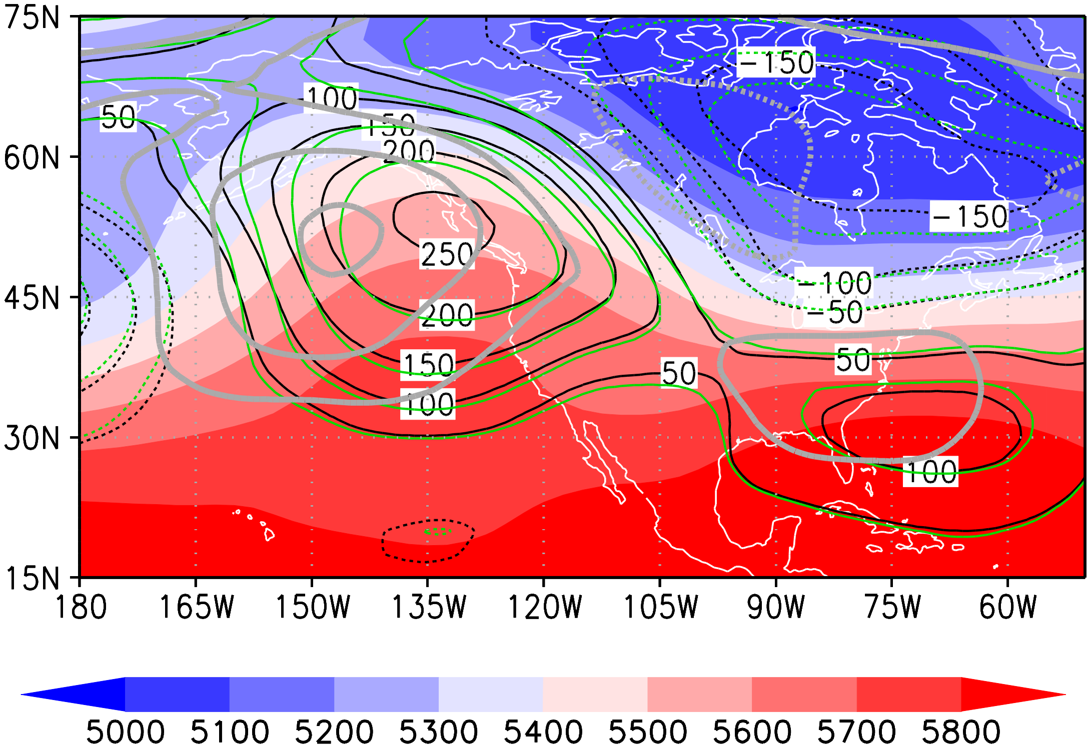

Fig. 1 500-hPa geopotential height (color shading in every 100 GPMs), two types of anomalies (contours) with (Z_a; green) or without (Z'; gray) climatological eddies, and daily eddies (Z^*; black) over Northeast Pacific and North America averaged during the PMZ episode in 9-26 January 2013. Contour interval is 50 GPMs with 0 being omitted.

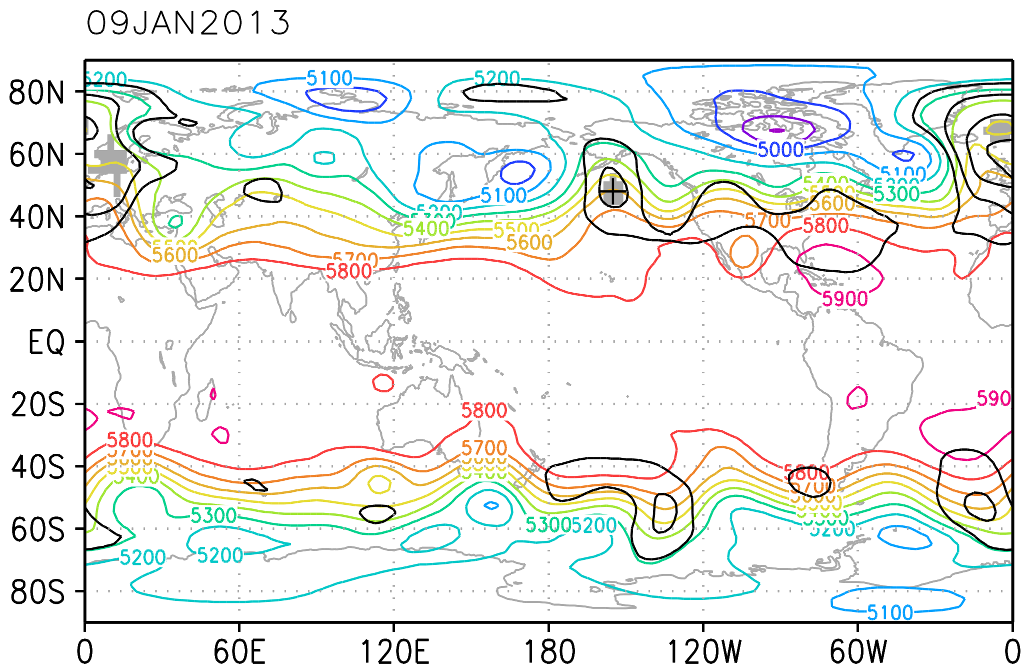

Fig. 2 A snapshot on 9 January 2013 for the identified maxima (gray shading) of different PMZ episodes. Contours in color or black are for the total field Z500 or Z* (starting from 100 GPMs) with an interval of 100 GPMs. The black cross indicates the intensity-weighted location of starting center in the northeast Pacific.

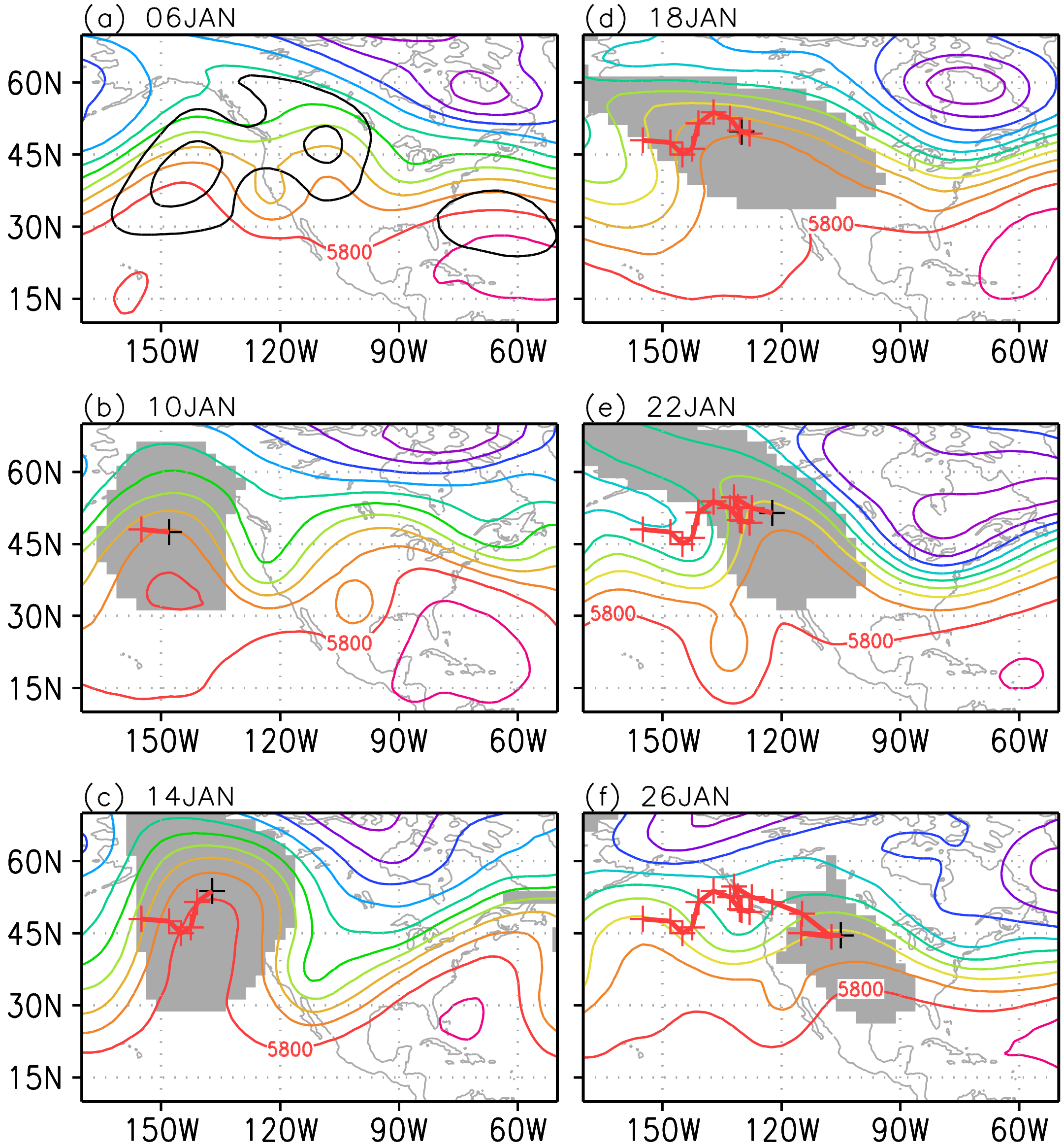

Fig. 3 Successive snapshots of intensity-weighted locations of PMZ cores during 9-26 January 2013. Black cross represents the core of current day and red ones for its predecessors, and gray shading is for the impact area of the PMZ on current day. Color contours are for the Z500 every 100 GPMs.

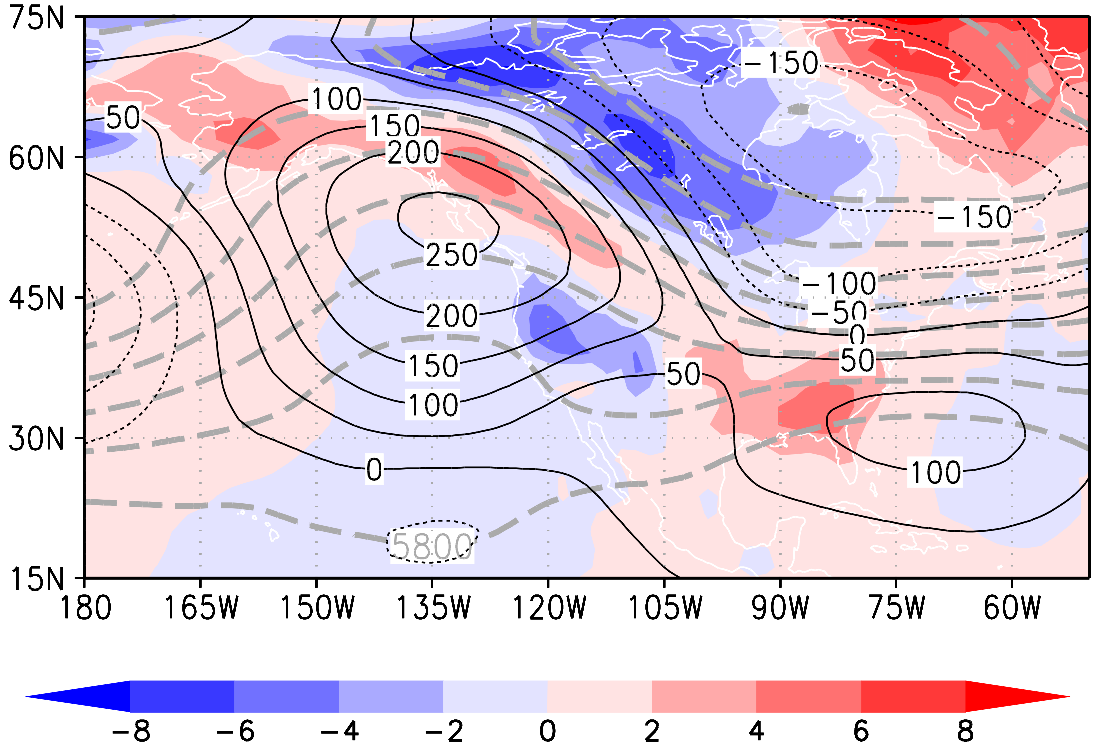

Fig. 4 Anomalies of 2-m temperature (color shading in K; T_s'), total 500-hPa geopotential height (gray-thick dashed isopleths; every 100 GPMs with the 5800 isopleth labeled; Z500), and daily eddies (black contours; Z^*) averaged during the blocking episode from 9-26 January 2013.

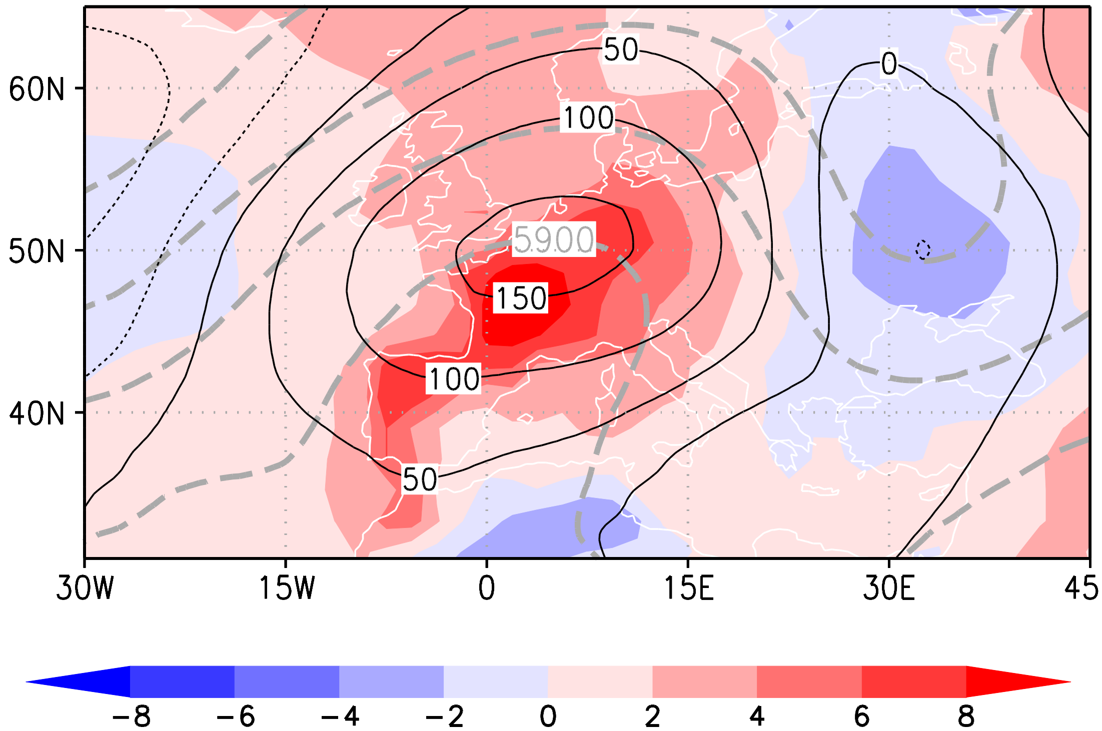

Fig. 5 Same as Fig. 4, but for the blocking episode associated with the record heatwave in Western Europe during 2-13 August 2003.

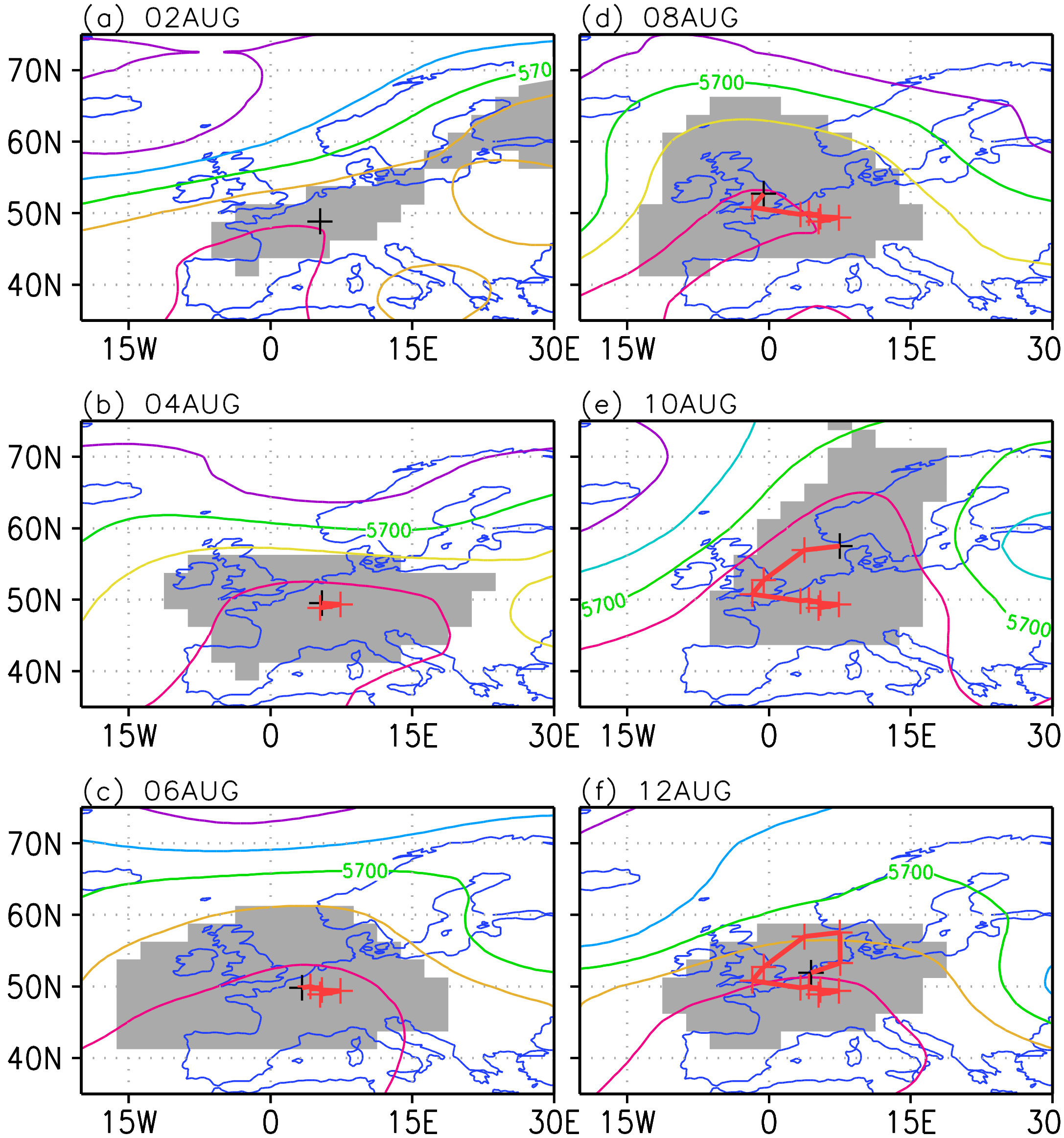

Fig. 6 Same as Fig. 3, but for persistent strong open ridges that occurred 2-12 August 2003 and caused the record heatwave in Western Europe.

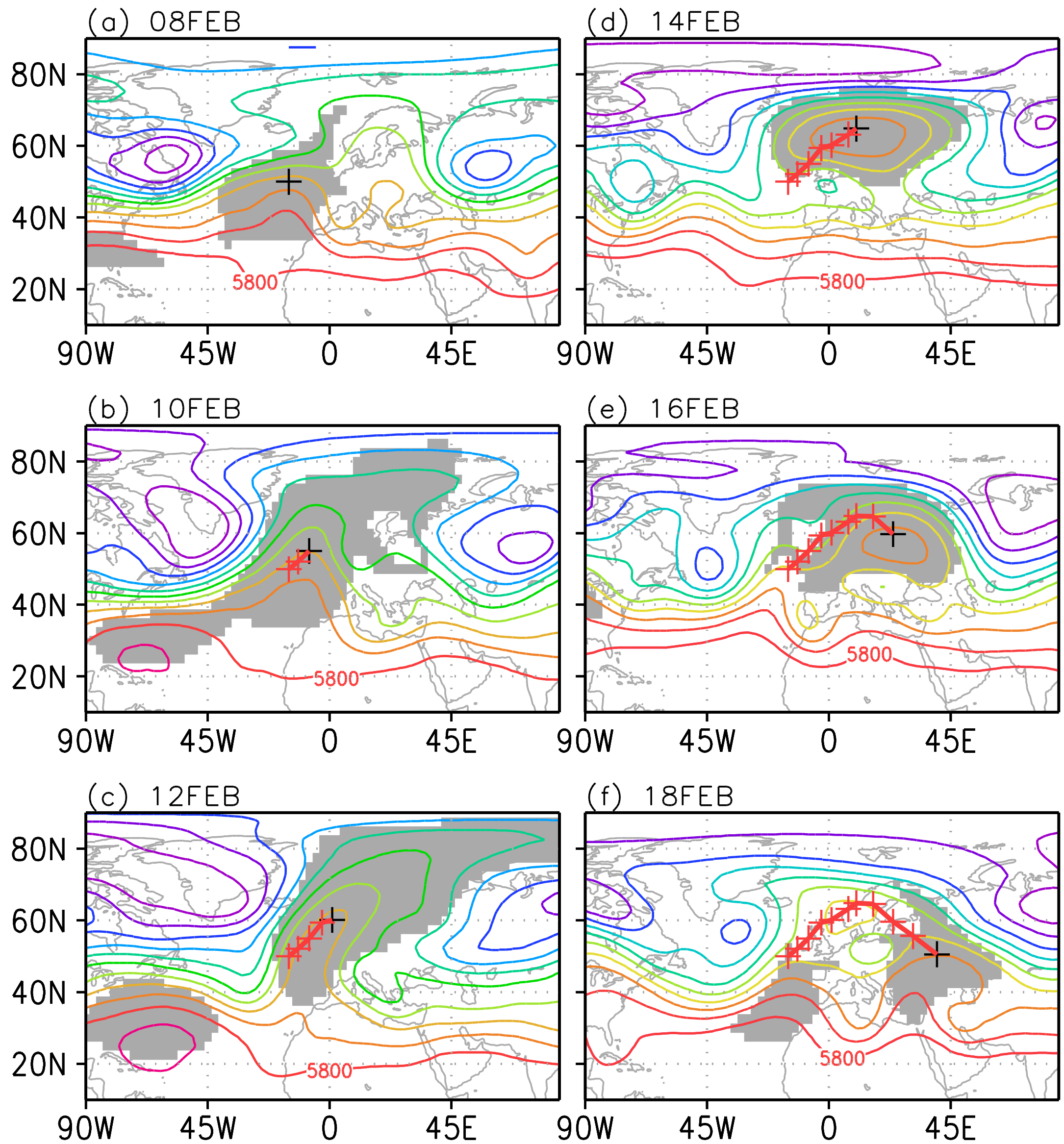

988

989 Fig. 7 Same as Fig. 3, but for a PMZ episode that evolved from an open ridge to an

990 omega-shape blocking, a cutoff high, and decayed back into an omega-shape blocking

991 during 8-18 February 1994.

992

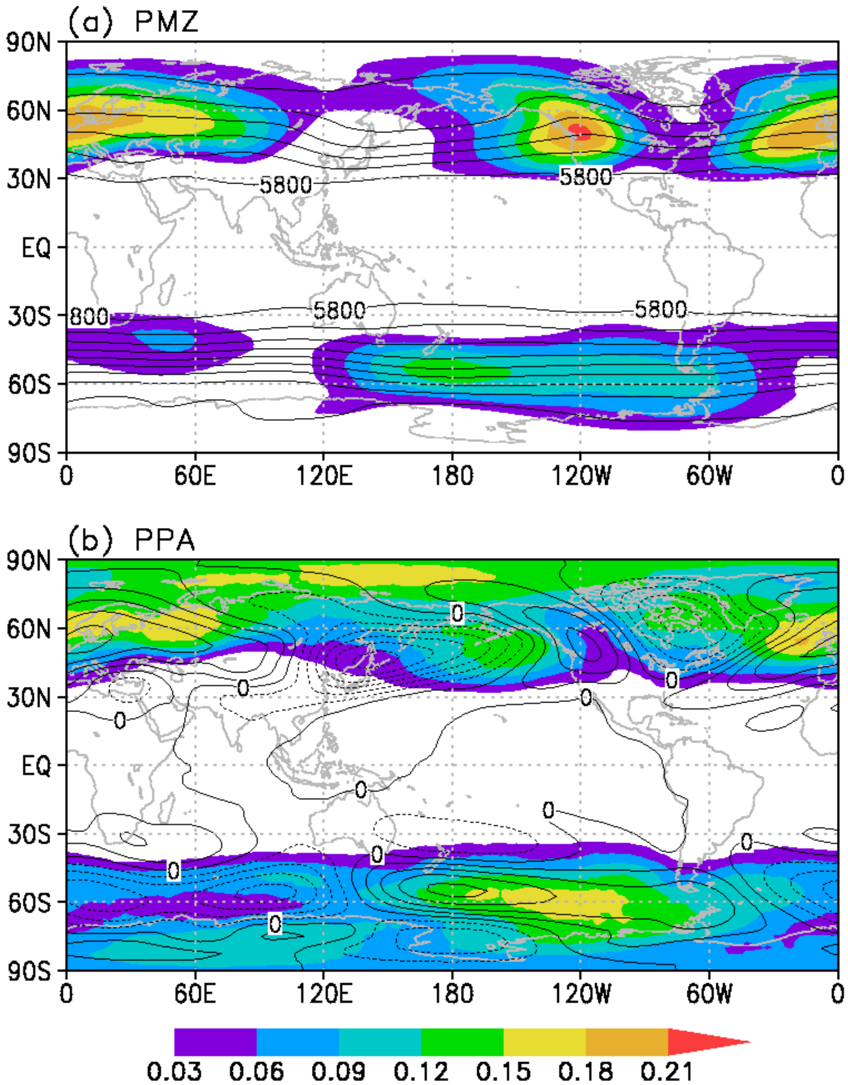

Fig. 8 Annual frequency distributions (color shading) for (a) the impact grid points of tracked PMZ events and (b) PPA days during all seasons from 1979-2015 super-imposed with all-time climatology in black contours for (a) Z500 starting at 5800 GPMs with an interval of 100 GPMs and (b) eddy anomalies Z* of (a) with an interval of 20 GPMs.

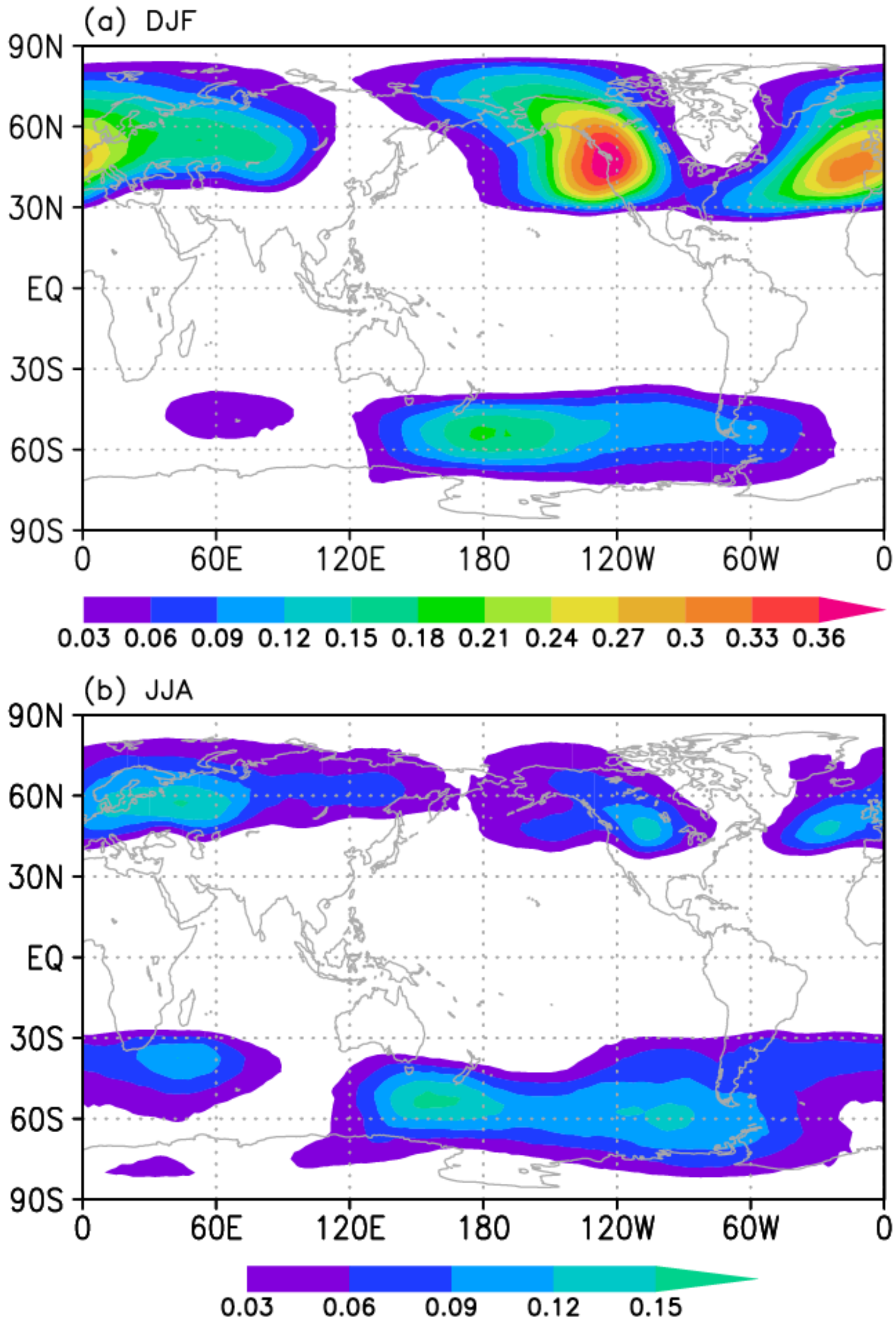

Fig. 9 Frequency distributions for the impact area of tracked PMZ events in DJF (a) and JJA (b).

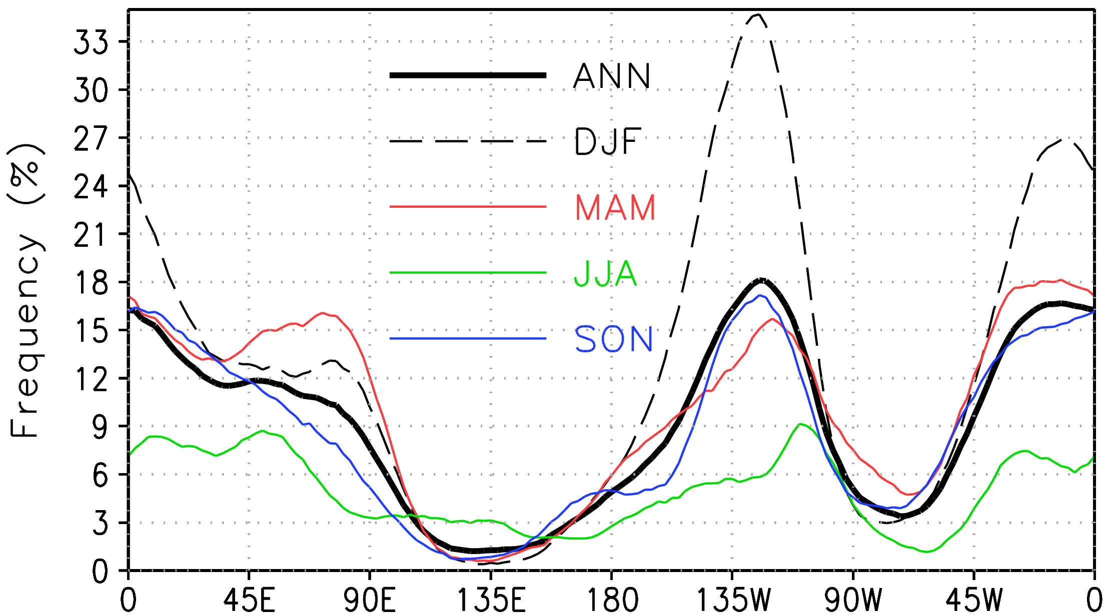

Fig. 10 Frequency distribution for the impact grid points of the tracked PMZ events between 1979-2015 for annual (solid black), seasonal DJF (black dashed), MAM (red), JJA (green), and SON (blue) averaged at the three latitudes of 40^{o}, 50^{o}, and 60^{o}N.

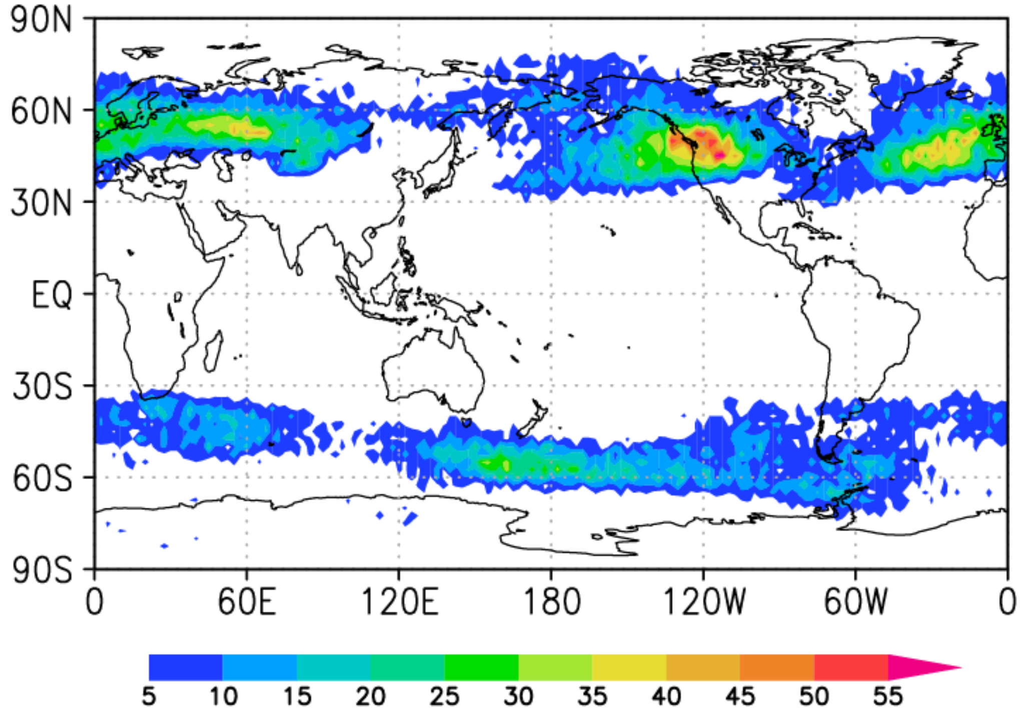

Fig. 11 Total number of PMZ cores during 1979-2015.

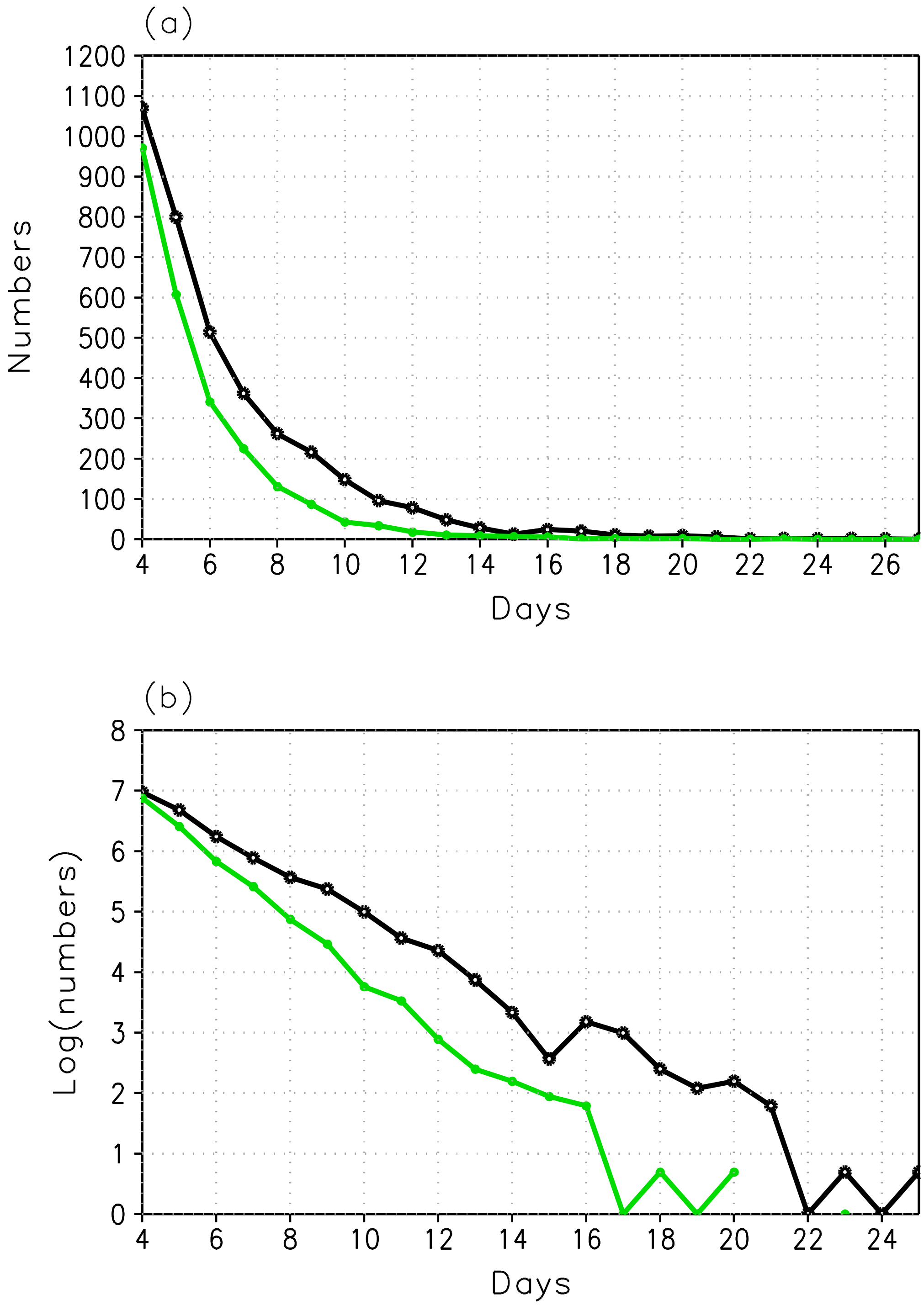

Fig. 12 Duration distributions for tracked PMZ events in the Northern (black) and Southern (green) Hemisphere during all seasons in 1979-2015. Panels (a) and (b) are for the total number of cores and its natural logarithm, respectively.

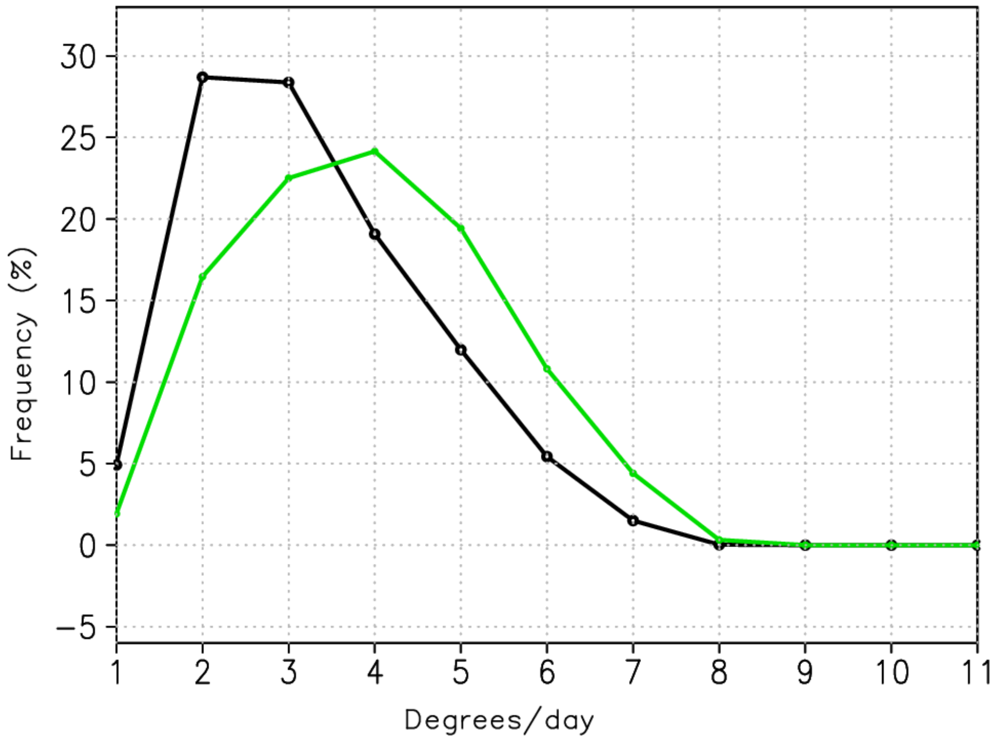

Fig. 13 Frequency distributions of averaged moving speed (degree in longitude per day) for tracked PMZ cores in the Northern (black) and Southern (green) Hemisphere during all seasons in 1979-2015.

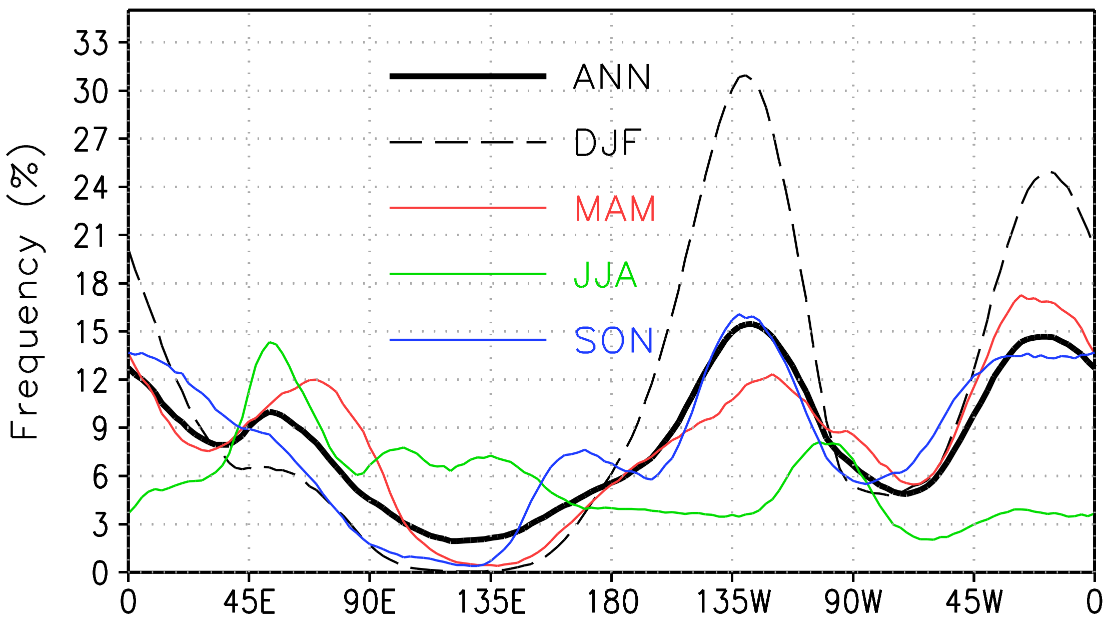

Fig. 14 Same as Fig. 11, but for the Z200 where the threshold of the core and impact grid points is 150 GPMs.

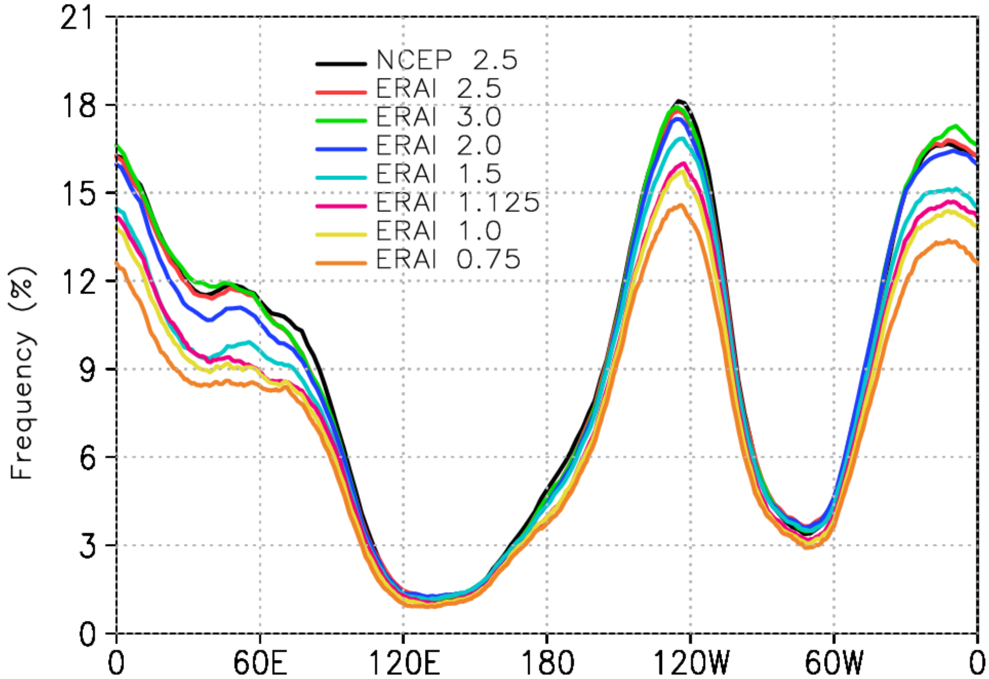

Fig. 15 Annual frequency distribution averaged at the three latitudes of 40°, 50°, and 60°N (closest latitudes otherwise) for the impact grid points of the tracked PMZ events between 1979-2015 based on the Z500 from the NCEP-NCAR Reanalysis at 2.5°×2.5° in longitude and latitude (black), ERA-Interim at 0.75°×0.75° (brown), 1.0°×1.0° (light blue), 1.125°×1.125° (purple), 1.5°×1.5° (light blue), 2.0°×2.0° (blue), 2.5°×2.5° (red), and 3°×3° (green), respectively.

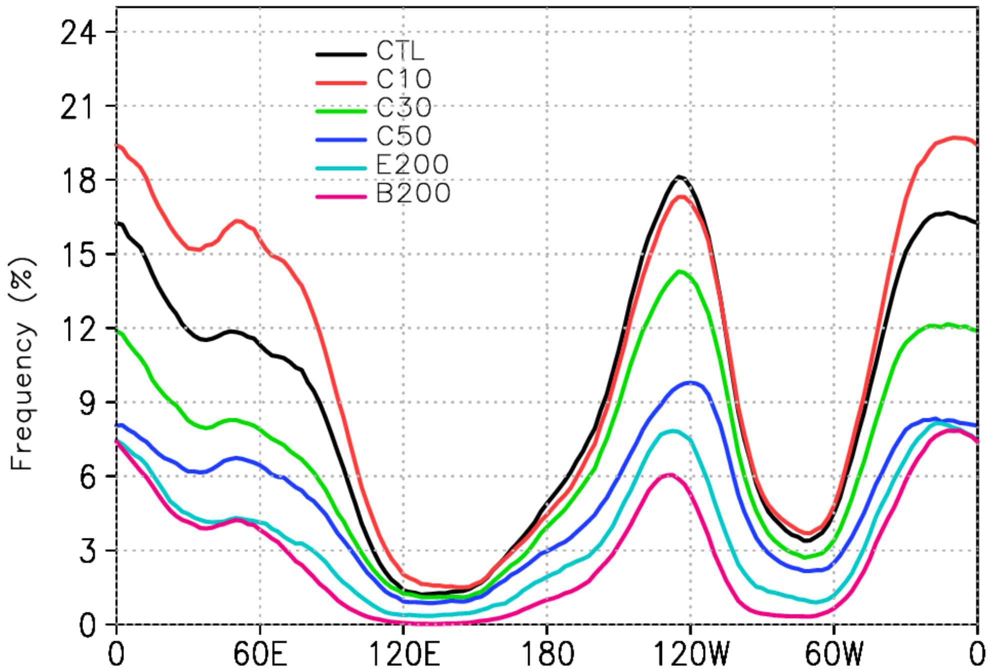

Fig. 16 Sensitivity to the thresholds in the annual frequency distribution averaged at the three latitudes of 40°, 50°, and 60°N for the impact grid points of the tracked PMZ events between 1979-2015 based on the Z500 from the NCEP-NCAR Reanalysis at 2.5°×2.5° in longitude and latitude for CTL (black), C10 (red), C30 (green), C50 (blue), E200 (light blue), and B200 (purple), respectively. See Table 4 for the thresholds in each case.